



Title	ANION AND CATION PARTITIONING BETWEEN ROCK-FORMING MINERAL PHASES
Author(s)	Yurimoto, Hisayoshi
Citation	Tsukuba University. 博士(理学)
Issue Date	1985-03-25
Doc URL	<a href="http://hdl.handle.net/2115/32893">http://hdl.handle.net/2115/32893</a>
Type	theses (doctoral)
File Information	yurimoto.pdf



[Instructions for use](#)

ANION AND CATION PARTITIONING BETWEEN ROCK-FORMING MINERAL PHASES

BY

HISAYOSHI YURIMOTO

THESIS

Submitted in partial fulfillment of the requirements  
for the degree of Doctor of Science  
in the Graduate College of the  
University of Tsukuba

1984

### Acknowledgements

The author gratefully acknowledges the expert guidance and supervision of Dr. Shigeo Sueno. His encouragement and support were exceedingly beneficial throughout my thesis research.

I am grateful to Prof. N. Onuma for his discussion, comments and critical reading of a part of the manuscript. I am thankful to Dr. H. Sato for giving us the valuable sample of DSDP. Special thanks are due to Prof. C. T. Prewitt who contributed greatly to improve the manuscript of chapter I by careful review. I also appreciate criticisms and comments on the manuscript by Drs. Y. Suzuki, T. Fujii, S. Shimoda, M. Kimata, S. Arai, J. A. Philpotts and I. M. Steele and Mrs. S. Matsuura and K. Watanabe at various stages of its preparation. Thanks are also due to Mrs. N. Nishida and K. Watanabe for technical assistance of EPMA and SIMS, respectively, and Dr. S. Arai for microscopic investigation.

### Abstract

Partition coefficients for -1, -2, -3, +1, +2, +3, +4 and +5 valent ions between the groundmass of tholeiite basalt and coexisting olivine and plagioclase phenocrysts from the Mid-Atlantic Ridge and between the groundmass of boninite and coexisting proto-, ortho-, C2/c pyroxenes and spinel phenocrysts have been determined by secondary ion mass spectrometry. The present cation partitioning strongly supports the "crystal structure control" mechanism. The partition coefficient for an anion is also under control of the crystal structure, so that each of the cation and anion positions in the crystal structure gives rise to a parabola-shaped peak on the partition coefficient vs. ionic radius diagram.

Partition coefficients for -1, -2, -3, +1, +2, +3, +4 and +5 valent ions between the exsolved blebby and the matrix pyroxenes in a websterite nodule from Takashima, Kyushu, Japan, have been also determined by secondary ion mass spectrometry. The partition coefficient for an ion between two pyroxene phases is expressed in term of the relative internal energy change of each crystal structure, so that the characteristic of partitioning between the exsolved and the matrix pyroxenes appears to be in general agreement with that of partitioning between coexisting pyroxene phenocrysts in igneous rock.

## CONTENTS

	Page
0. INTRODUCTION.....	1
I. PHENOCRYST/MAGMA PARTITIONING IN MID-OCEAN RIDGE BASALT.....	3
Experimental	3
Results	9
Discussion	17
II. PHENOCRYST/MAGMA PARTITIONING IN BONINITE.....	22
Experimental	22
Results	24
Discussion	38
III. EXSOLUTION/MATRIX PARTITIONING IN PYROXENE CRYSTALS OF ULTRAMAFIC NODULE.....	56
Experimental	56
Results	58
Discussion	66
IV SUMMARY.....	74
REFERENCES.....	76

	Table captions	page
Table I-1	Analytical details for elements of olivine, plagioclase and basaltic glass	6
Table I-2	Electron microprobe analyses of olivine rim, plagioclase rim and the adjacent groundmass glass	10
Table I-3	Relative ion intensities of SIMS analyses of phenocryst rim and the adjacent groundmass glass	12
Table I-4	Partition coefficients of the elements between phenocrysts and groundmass	15
Table II-1	Electron microprobe analyses of phenocrysts and the coexisting groundmass glass in boninite	32
Table II-2	Relative ion intensities of SIMS analyses for phenocrysts and the coexisting groundmass glass in boninite	33
Table II-3	Partition coefficients of the elements between phenocrysts and groundmass in boninite	35
Table II-4	Comparison of the mean interatomic distances (pm) in pyroxenes and spinel	43
Table III-1	Electron microprobe analyses of exsolution and the matrix pyroxenes	59
Table III-2	Relative ion intensities of SIMS analyses for exsolution and the host pyroxenes	61
Table III-3	Partition coefficients of the elements between exsolution and the host pyroxenes	63

## Figure captions

page

Fig. I-1	<p>Partition coefficient-ionic radius diagram for olivine-groundmass system.</p> <p>⊙: +1 valent ions, ⊖: +2 valent ions, ⊗: +3 valent ions, □: +4 valent ions, ■: +5 valent ions, △: -1 valent ions, ▲: -2 valent ions, ▼: -3 valent ions.</p> <p>Above ions were measured using secondary positive-ion detection of SIMS except for 0 ion. The partition coefficient of 0 was calculated from EPMA Data.</p> <p>▽: -1 valent ions, ▽: -2 valent ions,</p> <p>Above ions were measured using secondary negative-ion detection of SIMS.</p>	18
Fig. I-2	<p>Partition coefficient-ionic radius diagram for plagioclase-groundmass system. Symbols are the same as in Fig. 1.</p>	19
Fig. II-1	<p>Electron microprobe traces across contact between bronzite and glass. (A) CJ-02A, (B) CJ-02B</p>	25
Fig. II-2	<p>Electron microprobe traces across contact between epitaxial bronzite and glass.</p>	26
Fig. II-3	<p>Electron microprobe traces across contact between augite and glass. (A) CJ-02A, (B) CJ-02B</p>	29
Fig. II-4	<p>Electron microprobe traces across contact between spinel and glass.</p>	30

- Fig. II-5      The relation between the relative secondary ion intensity and the partition coefficient measured by EPMA.
- △: Olivine/groundmass (Yurimoto and Sueno 1984a)
- ▽: Olivine/groundmass (Yurimoto and Sueno, unpublished)
- : Plagioclase/groundmass (Yurimoto and Sueno 1984a)
- : Bronzite/augite (Chapter III)
- : Protoenstatite/groundmass (This study)
- ▣: Bronzite/groundmass (This study)
- ▲: Augite/groundmass (This study)
- : Chrome spinel/groundmass (This study) 36
- Fig. II-6      Partition coefficient-ionic radius diagram for  
bronzite-groundmass system. (A) CJ-02A, (B) CJ-02B  
and (C) CJ-02C. Symbols are the same as in Fig. I-1. 40
- Fig. II-7      Partition coefficient-ionic radius diagram for  
protoenstatite-groundmass system. Symbols are the same  
as in Fig. I-1. 45
- Fig. II-8      Partition coefficient-ionic radius diagram for  
augite-groundmass system. (A) CJ-02A and (B) CJ-02B.  
Symbols are the same as in Fig. I-1. 49
- Fig. II-9      Partition coefficient-ionic radius diagram for  
spinel-groundmass system. Symbols are the same as in  
Fig. I-1. 51



- Fig. III-1 (a) Transmitted light photomicrograph of exsolved pyroxens from specimen TKW-03. The length of the scale bar is 0.3 mm. Under polarized light. Aug=augite. Brz=bronzite. (b) Transmitted light photomicrograph of specimen TKW-03-A. The length of the scale bar is 20  $\mu\text{m}$ . Under polarized light.
- ☆=trace of primary beam of SIMS analysis.
- (c) Transmitted light photomicrograph of specimen TKW-03-B. The length of the scale bar is 20  $\mu\text{m}$ . Under polarized light. 57
- Fig. III-2 The relation between the relative secondary ion intensity and the partition coefficient measured by EPMA.
- △: Olivine/Groundmass (Yurimoto and Sueno, 1984a)
- ▽: Plagioclase/groundmass (Yurimoto and Sueno, 1984a)
- : TKW-03-A (This study)
- : TKW-03-B (This study) 65
- Fig. III-3 Partition coefficient-ionic radius diagram for TKW-03-A. Symbols are the same as in Fig. I-1. 67
- Fig. III-4 Partition coefficient-ionic radius diagram for TKW-03-B. Symbols are the same as in Fig. I-1. 68
- Fig. III-5 Partition coefficient-ionic radius diagram for augite-bronzite phenocrysts (after Matsui et al., 1977). Symbols are the same as in Fig. I-1. 72

## 0. INTRODUCTION

Element partitioning between minerals and magma has been one of the most fundamental factors for discussing the evolution of Earth. Especially the partition coefficients for olivine-, pyroxene-, chrome spinel-, and plagioclase-silicate magma systems would be most important for discussing the distribution of element in upper mantle because most of upper mantle materials occupied by those minerals.

Onuma et al. (1968) found that partition coefficients for cations between pyroxenes (augite and bronzite) and groundmass formed parabola-shaped peaks on partition coefficient-ionic radius (PC-IR or Onuma) diagrams, and similar peaks on PC-IR diagrams have been reported for other mineral/groundmass systems (Higuchi and Nagasawa, 1969; Jensen, 1973; Matsui et al., 1977; Philpotts, 1978; Onuma et al., 1981). The results give strong support to the idea proposed by Onuma et al. (1968) that each type of coordination polyhedron around cations gives rise to a parabola-shaped peak for cations with the same valency on the PC-IR diagram and each peak tends to parallel those for ions of other valences. Further Onuma et al. (1968) proposed that the positions of peak-tops for a given site can be regarded as being characteristic of the structure of the relevant mineral. The theoretical treatment was done on the basis of simple isotropic bulk strain model (Nagasawa, 1966) or ionic lattice strain model (Tsang et al., 1978). Matsui et al. (1977) termed the idea as "crystal structure control."

The behavior of anion partitioning between mineral and groundmass, which is important for discussing magma genesis, on PC-IR diagrams has not yet been reported. Further the partition coefficients of the previous works has been measured by bulk analysis of each phenocryst and groundmass after phase separation. The previous method only assumed that the separated phenocryst and groundmass are in equilibrium, though the zoning and inclusions are common features in phenocrysts which do not favor this assumption. However, the analysis using secondary ion mass spectrometry (SIMS) can analyze major and trace elements (including anions) in a micro area of material. Therefore, in SIMS analysis, it is possible to evaluate whether equilibrium is achieved or not on either side of phenocryst/groundmass contact.

In this paper, we have measured mineral/groundmass partition coefficients of many anions and cations in mid-ocean ridge basalt and boninite and measured exsolution/matrix partition coefficients for pyroxene using SIMS. This report is to present PC-IR diagram of olivine, protoenstatite, bronzite, augite, plagioclase and chrome spinel, and discuss how anions and cations are distributed, how element partitioning changes by the bulk chemistry of the system and how the differences of partition coefficients are determined between mineral phases. This is the first report of PC-IR diagrams that include anions.

## I. PHENOCRYST/MAGMA PARTITIONING IN MID-OCEAN RIDGE BASALT

### Experimental

#### Sample

Almost all anions are among the so-called volatile elements, so that for minimizing the effect of possible degassing of volatile elements from magma during and after eruption and later secondary contamination, a quenched-rim part of mid-ocean ridge basalt was used for the sample of the SIMS experiments. The sample is a phyric olivine-plagioclase basalt that consists of clear basaltic glass and crystals, from Hole 396B, IOPD/DSDP Leg 46; the petrography was described previously (Sato et al., 1978). Mineral/groundmass partition coefficients are based on measurements on both sides of the mineral-glass boundary using SIMS and an electron micro-probe analyzer (EPMA).

#### SIMS Analysis

The instrument used in this study was the Cameca IMS-3f ion microanalyzer at the Chemical Analysis Center of the University of Tsukuba. The vacuum of the sample chamber and the mass spectrometer were maintained at 3 and 0.5  $\mu$ Pa, respectively, during the measurement. Oxygen gas with a purity of more than 99.99% was supplied to the duoplasmatron to generate the primary ion beam which was mostly composed of negatively charged monovalent oxygen ( $O^-$ ) ions.

The primary high voltage used in this study was 9.3 kV for

secondary positive-ion detection and 12.0 kV for secondary negative-ion detection. The secondary high voltage used was 4.5 kV for both detection. Therefore, the net primary ion beam accelerating energy was 13.8 keV (for the secondary positive-ion) and 7.5 keV (for the secondary negative-ion). The beam was focused on the sample surface with a diameter of 15-20  $\mu\text{m}$  on the gold-coated surface of a polished thin section and the current was ranging from 5 to 10 nA. For instrumental reasons, it was not possible to monitor the fluctuations of the primary beam current during the analysis. However, since the drift of the primary beam current was less than 2% for a current measurement of over 10 minutes, the average of the current values measured before and after the analysis for a isotope could be used with satisfactory accuracy as the primary beam current value during the analysis.

The secondary ions were measured by an electron multiplier coupled with pulse-counting circuitry. Dead time of the electron multiplier was measured as 50 ns and the corrections were negligible for count rates less than  $10^6$  counts/s. Background of the electron multiplier was  $0.2 \pm 0.1$  counts/s.

One of the major problems to SIMS analysis for most oxide materials is the large abundance of molecular ions. The possible interferences on olivine, plagioclase and basaltic glass with a mass resolution over about 4000 are listed in Table I-1. In this table, the degree of interferences are calculated based on the observations and the natural isotopic abundances. In this experimental condition, single charged oxide and hydride interferences were less than 1% of the monatomic ion intensities and dimer molecules were less than 0.1% of the monatomic ion

intensities. Single charged carbide interferences were not observed and more complex ion species are expected to be less than 0.01% of the monatomic ion intensities. In order to eliminate the effect of the molecular-ion interferences, the secondary ion intensities were counted on the flat topped peak with a mass resolution (10% valley) of about 5000. The secondary ion signals attained to stable levels within several minutes after starting the bombardment of the primary beam, and this level was generally maintained during the measurement.

The following procedures were employed for SIMS analysis:

The basalt sample was mounted on a slide glass by epoxy cement. The mounted sample was sliced by a diamond cutter and ground to thin section on SiC paper and polished with 1  $\mu$ m alumina powder in distilled water. After the final polishing, the sample surface was cleaned ultrasonically in alcohol and then distilled water, and dried immediately in a vacuum chamber. In order to eliminate the electric charge on the surface during the analysis, the polished surface of the sample was coated with a gold layer of about 15 nm in thickness using a vacuum evaporator.

Positive secondary ion intensity ratios relative to  $^{28}\text{Si}$  were measured for Li, Na, K, Mg, Ca, Mn, Fe, Co, Ni, Cu, Zn, Sr, Cd, Ba, B, Al, Sc, V, Cr, Ga, Y, La, Ce, C, Ti, Ge, Zr, P, As, H, F, O, S and N. Negative secondary ion intensity ratios relative to  $^{28}\text{Si}$  were measured for H, F, Cl, O and S. The secondary ions were counted in the range from 3 to 50 seconds for each isotope. The intensity of  $^{28}\text{Si}$  was measured after the measurement of every four or five different elements in order to monitor the instrumental stability.

Table I-1 Analytical details for elements of olivine, plagioclase and basaltic glass

Isotope	% Abundance	possible Interference*	M/ $\Delta$ M	Comments
$^1\text{H}$	99.985	—	—	Background H contamination may be 1000 counts/sec at $10^{-6}$ Pa on Si single crystal. The background intensity is below 20 % of H count rate in this study.
$^7\text{Li}$	92.5	—	—	
$^{11}\text{B}$	81.3	—	—	
$^{12}\text{C}$	98.89	—	—	Background C contamination is not observed on Si single crystal.
$^{14}\text{N}$	99.635	$^{14}\text{C}$	+82E3	Background N contamination is not observed on Si single crystal. $^{14}\text{C}$ is not observed because of the low concentration of carbon in natural silicate.
$^{16}\text{O}$	99.759	—	—	Problem with background O contamination from primary beam. Background counts are 1000 counts/sec on Si single crystal with a few nano-amperes of primary beam at $10^{-6}$ Pa. The O signal from the sample is difficult to observe due to the background.
$^{19}\text{F}$	100.00	—	—	
$^{23}\text{Na}$	100.00	$^{30}\text{Si}^{16}\text{O}^{2+}$	-4246	SiO interference can be separated.
$^{26}\text{Mg}$	11.29	—	—	
$^{27}\text{Al}$	100.00	$\text{MgSi}^{2+}$	-68E3	MgSi interference is absent because $\text{MgSi}^{2+}$ intensity is not observed at $m/e=26.5$ .
$^{28}\text{Si}$	92.18	—	—	
$^{29}\text{Si}$	4.71	—	—	
$^{30}\text{Si}$	3.12	—	—	
$^{31}\text{P}$	100.00	$^{30}\text{SiH}^+$ $^{30}\text{SiO}_2^{2+}$	+3961 +3880	Both SiH and $\text{SiO}_2$ interferences can be separated.

Table I-1 (continued)

Isotope	% Abundance	possible Interference*	M/ΔM	Comments
$^{32}\text{S}$	95.018	$^{64}\text{Ni}^{2+}$ $^{64}\text{Zn}^{2+}$	-3952 -4263	Ni interference is absent because $^{61}\text{Ni}^{2+}$ interference is not observed at $m/e=30.5$ . Zn interference is absent judging from the low intensity of $\text{Zn}^+$ .
$^{35}\text{Cl}$	75.53	$^{34}\text{SH}^-$	+5120	SH interference is less than 0.1% of F count rate.
$^{39}\text{K}$	93.08	$^{24}\text{Mg}^{56}\text{Fe}^{2+}$	-28E3	MgFe interference observed at $m/e=40.5$ is less than 5 counts/sec. Therefore, the interference is less than 10% of K count rate.
$^{40}\text{Ca}$	96.96	$^{24}\text{Mg}^{56}\text{Fe}^{2+}$ $^{40}\text{K}^+$ $^{39}\text{KH}^+$	-15E3 +28E3 +4470	MgFe interference is less than 50 counts/sec judging from the counts at $m/e=40.5$ . K interference is less than a few counts/sec and it is negligible. KH interference is less than 1% of Ca count rate. Total count rate of the interferences is less than 1% of Ca count rate.
$^{45}\text{Sc}$	100.00	$^{44}\text{CaH}^+$	+6705	CaH interference is less than 10% of Sc count rate.
$^{47}\text{Ti}$	7.32	$^{46}\text{TiH}^+$	+5403	TiH interference is less than 1% of Ti count rate.
$^{51}\text{V}$	99.76	—	—	
$^{52}\text{Cr}$	83.76	$^{51}\text{VH}^+$	+4601	VH interference can be separated.
$^{55}\text{Mn}$	100.00	$^{54}\text{CrH}^+$ $^{54}\text{FeH}^+$	+6359 +5857	CrH and FeH interferences are less than 0.1% and 5% of Mn count rate respectively.
$^{56}\text{Fe}$	91.68	$^{55}\text{MnH}^+$	+5118	MnH interference is less than 0.01% of Fe count rate.
$^{59}\text{Co}$	100.00	$^{58}\text{FeH}^+$ $^{58}\text{NiH}^+$	+7413 +5899	Both FeH and NiH interferences are less than 1% of Co count rate.
$^{60}\text{Ni}$	26.2	$^{59}\text{CoH}^+$	+5858	CoH interference is less than 0.05% of Ni count rate.
$^{63}\text{Cu}$	69.1	$^{62}\text{NiH}^+$	+9578	NiH interference is less than 10% of Cu count rate.



Table I-1 (continued)

Isotope	% Abundance	possible Interference*	M/ $\Delta$ M	Comments
$^{66}\text{Zn}$	27.81	$^{65}\text{CuH}^+$ $^{50}\text{TiO}^+$ $^{50}\text{CrO}^+$	+6903 +4829 +4422	CuH interference is less than 1% of Zn count rate. TiO and CrO interferences can be separated.
$^{69}\text{Ga}$	60.2	$^{68}\text{ZnH}^+$ $^{53}\text{CrO}^+$	+9889 +6998	ZnH and CrO interferences are less than 1% and 10% of Ga count rate.
$^{74}\text{Ge}$	36.74	$^{58}\text{FeO}^+$ $^{58}\text{NiO}^+$ $^{56}\text{Fe}^{18}\text{O}^+$	+10E3 +7983 +7319	Interference mainly due to NiO. NiO interference may intense relative to Ge count rate.
$^{75}\text{As}$	100.00	$^{59}\text{CoO}^+$ $^{74}\text{GeH}^+$ $^{48}\text{TiAl}^+$ $^{57}\text{Fe}^{18}\text{O}^+$	+12E3 +11E3 +9630 +5812	CoO, GeH, TiAl and FeO interferences are less than 5, 1, 10 and 1% of As count rate.
$^{88}\text{Sr}$	82.5	$^{40}\text{Ca}^{48}\text{Ti}^+$ $^{88}\text{Ca}^+$ $^{56}\text{Ca}_2^+$ $^{56}\text{FeO}_2^+$	+18E3 +8348 +5585	CaTi, $\text{Ca}_2$ and $\text{FeO}_2$ interferences are less than 1% of Sr count rate.
$^{89}\text{Y}$	100.00	$^{88}\text{SrH}^+$ $^{57}\text{FeO}_2^+$	+11E3 +4562	SrH and FeO interferences are less than 1% of Y count rate.
$^{90}\text{Zr}$	51.46	$^{89}\text{YH}^+$ $^{58}\text{NiO}_2^+$	+9762 +4318	YH and NiO interferences are less than 1% of Zr count rate.
$^{114}\text{Cd}$	28.86	$^{113}\text{CdH}^+$	+12E3	CdH interference is less than 1% of Cd count rate.
$^{138}\text{Ba}$	71.66	$^{137}\text{BaH}^+$	+16E3	BaH interference is less than 1% of Ba count rate.
$^{139}\text{La}$	99.911	$^{138}\text{BaH}^+$	+20E3	BaH interference is less than 1% of La count rate.
$^{140}\text{Ce}$	88.48	$^{140}\text{LaH}^+$	+16E3	LaH interference is less than 1% of Ce count rate.

Some isotope ratios of elements are also checked by the natural isotope abundance. \* over  $M/\Delta M \approx 4000$ .

## EPMA Analysis

The EPMA instrument used in this study is a computer-controlled electron probe X-ray micro-analyzer at the Chemical Analysis Center of the University of Tsukuba. The EPMA system, which consists of a JXA50A (JEOL) main part and an ACPS-XR (ELIONIX) controlling part, was used with an accelerating voltage of 15 kV and a probe current of 0.014  $\mu$ A on a Faraday cage. A beam spot of about 1-2  $\mu$ m in diameter was used. Standards used were  $\text{SiO}_2$  for Si,  $\text{Al}_2\text{O}_3$  for Al,  $\text{TiO}_2$  for Ti,  $\text{Cr}_2\text{O}_3$  for Cr,  $\text{Fe}_2\text{O}_3$  for Fe, NiO for Ni,  $\text{MnFe}_2\text{O}_4$  for Mn, MgO for Mg,  $\text{CaSiO}_3$  for Ca,  $\text{NaAlSi}_3\text{O}_8$  for Na, and  $\text{KAlSi}_3\text{O}_8$  for K. The Bence and Albee (1968) method was used to make quantitative analysis corrections. Other experimental procedures were similar to those employed by Nishida *et al.* (1979).

## Results

EPMA line analyses across the contact between the phenocrysts and the groundmass glass showed no detectable composition gradients for major elements on either side of the contact; the chemical compositions of each side are shown in Table I-2. This evidence shows that the equilibrium is achieved between the phenocryst rim and groundmass in both olivine- and plagioclase- groundmass systems. These equilibrium parts were also analyzed by SIMS. Relative secondary ion intensities for the phenocryst rim and the adjacent groundmass glass are listed in Table I-3.

Table I-1 summarizes the systematic examination of interferences to analytical peaks. The effects of interferences are less than 10% (mostly 5%) of the objective monatomic ion intensities except for H, O

Table I-2 Electron microprobe analyses of  
olivine rim, plagioclase rim and the adjacent  
groundmass glass

	O1	P1	Grm
SiO <sub>2</sub>	39.7 $\pm$ 0.2 <sup>†</sup>	47.7 $\pm$ 0.4	50.3 $\pm$ 0.4
TiO <sub>2</sub>	-	-	1.47 $\pm$ 0.05
Al <sub>2</sub> O <sub>3</sub>	-	32.5 $\pm$ 0.2	15.1 $\pm$ 0.2
FeO*	13.8 $\pm$ 0.3	0.40 $\pm$ 0.06	9.3 $\pm$ 0.4
MnO	0.25 $\pm$ 0.05	-	0.18 $\pm$ 0.04
MgO	45.9 $\pm$ 0.2	0.24 $\pm$ 0.03	7.8 $\pm$ 0.1
CaO	0.30 $\pm$ 0.02	16.2 $\pm$ 0.2	11.4 $\pm$ 0.2
Na <sub>2</sub> O	-	2.33 $\pm$ 0.05	3.0 $\pm$ 0.1
K <sub>2</sub> O	-	-	0.09 $\pm$ 0.02
Total	100.0	99.4	98.6

O1 = olivine, P1 = plagioclase,  
Grm = groundmass. The major compositions  
of both the adjacent groundmass have the  
same values.

\* total iron as FeO. † Standard deviation.

and Ge, so that the correction for the interferences is neglected. Hydrogen background intensity may be below 20% of H peak. However, the correction for the background is neglected because the absolute level is uncertain due to lack of standards. Oxygen background level may be intense relative to oxygen peak from the samples. Germanium peak may be overlapped with NiO interference. Therefore, the secondary ion intensities for O and Ge are eliminated from the discussion below.

Quantitative chemical analysis using SIMS is still difficult because of the existence of various kinds of mutual interference in the emission of the secondary ions (Shimizu and Hart, 1982). However, some investigations have been made which indicate that an empirical approach is useful for quantitative analysis for silicates (e.g. Shimizu et al., 1978; Steele et al., 1981; Ray and Hart, 1982). The calibration curves reported previously show that the secondary ion intensities are generally proportional to the concentration of the element for many major and trace elements. It has been reported that the secondary ion intensity of  $^1\text{H}$  is proportional to water content or  $\text{OH}^-$  concentration in minerals and glasses (Hinthorne and Andersen, 1975; Delaney and Karsten, 1981). Therefore, it is possible to consider that the relative secondary ion intensities (Table I-3) are proportional to the concentration of the element and that the intensity of  $^1\text{H}$  indicates the concentration of  $\text{OH}^-$  in this study, although the background intensity may be below 20% (Table I-1).

Partition coefficient values calculated from the values in Tables I-2 and I-3 are listed in Table I-4 and plotted in Figs. I-1 and I-2. The partition coefficient(D) of a particular element is defined as the

Table I-3. Relative ion intensities of SIMS analyses of phenocryst rim  
and the adjacent groundmass glass

Element	Relative secondary ion intensity					
	Groundmass		Olivine	Groundmass		Plagioclase
<sup>7</sup> Li	8.37	$\times 10^{-4}$	$4.64 \pm 0.74 \times 10^{-4}$	$9.82 \pm 0.58 \times 10^{-4}$	1.28	$\times 10^{-4}$
<sup>23</sup> Na	1.57		$7.77 \times 10^{-3}$	1.94	1.11	
<sup>39</sup> K	5.46	$\times 10^{-2}$	$1.76 \pm 0.32 \times 10^{-4}$	$7.43 \times 10^{-2}$	1.00	$\times 10^{-2}$
<sup>26</sup> Mg	1.38	$\times 10^{-1}$	1.18	$1.45 \times 10^{-1}$	3.90	$\times 10^{-3}$
<sup>40</sup> Ca	2.22		$9.97 \times 10^{-2}$	2.42	3.19	
<sup>55</sup> Mn	1.14	$\times 10^{-2}$	$1.71 \times 10^{-2}$	$1.23 \times 10^{-2}$	$2.53 \pm 0.37 \times 10^{-4}$	
<sup>56</sup> Fe	4.03	$\times 10^{-1}$	$7.22 \times 10^{-1}$	$4.39 \times 10^{-1}$	1.33	$\times 10^{-2}$
<sup>59</sup> Co	$2.13 \pm 0.13 \times 10^{-4}$		$8.35 \times 10^{-4}$	$2.31 \times 10^{-4}$	$4.6 \pm 1.8 \times 10^{-6}$	
<sup>60</sup> Ni	5.98	$\times 10^{-3}$	$1.00 \times 10^{-2}$	$7.39 \times 10^{-3}$	4.09	$\times 10^{-3}$
<sup>63</sup> Cu	$1.45 \pm 0.15 \times 10^{-4}$		$1.76 \pm 0.75 \times 10^{-5}$	$1.62 \pm 0.11 \times 10^{-4}$	$1.03 \pm 0.31 \times 10^{-5}$	
<sup>66</sup> Zn	$2.57 \pm 0.52 \times 10^{-5}$		$3.11 \pm 0.42 \times 10^{-5}$	$2.92 \times 10^{-5}$	-	
<sup>88</sup> Sr	1.01	$\times 10^{-3}$	$1.40 \pm 0.43 \times 10^{-5}$	$1.19 \times 10^{-3}$	2.37	$\times 10^{-3}$
<sup>114</sup> Cd	$8.38 \pm 0.88 \times 10^{-5}$		-	$1.19 \pm 0.16 \times 10^{-4}$	$9.95 \pm 0.23 \times 10^{-5}$	
<sup>138</sup> Ba	$2.77 \pm 0.24 \times 10^{-5}$		-	$3.10 \pm 0.46 \times 10^{-5}$	$7.7 \pm 1.9 \times 10^{-6}$	
<sup>11</sup> B	$1.18 \pm 0.12 \times 10^{-5}$		-	$1.28 \times 10^{-5}$	$1.15 \pm 0.21 \times 10^{-5}$	
<sup>27</sup> Al	1.56		$9.00 \times 10^{-3}$	1.66	3.07	
<sup>45</sup> Sc	5.41	$\times 10^{-4}$	$1.66 \pm 0.24 \times 10^{-4}$	$5.86 \pm 0.32 \times 10^{-4}$	$9.9 \pm 0.30 \times 10^{-6}$	
<sup>51</sup> V	1.46	$\times 10^{-3}$	$5.7 \pm 1.7 \times 10^{-5}$	$1.47 \times 10^{-3}$	$1.37 \pm 0.45 \times 10^{-5}$	
<sup>52</sup> Cr	2.02	$\times 10^{-3}$	$1.55 \times 10^{-3}$	$2.18 \times 10^{-3}$	$2.56 \pm 0.64 \times 10^{-5}$	
<sup>69</sup> Ga	$7.31 \pm 0.49 \times 10^{-5}$		-	$8.90 \pm 0.70 \times 10^{-5}$	$5.6 \pm 1.0 \times 10^{-5}$	
<sup>89</sup> Y	$9.40 \pm 0.74 \times 10^{-5}$		-	$1.14 \times 10^{-4}$	$3.61 \pm 0.11 \times 10^{-6}$	
<sup>139</sup> La	$2.69 \pm 0.32 \times 10^{-5}$		-	$4.25 \pm 0.65 \times 10^{-5}$	$6.3 \pm 1.4 \times 10^{-6}$	
<sup>140</sup> Ce	$4.42 \pm 0.36 \times 10^{-5}$		-	$5.30 \pm 0.75 \times 10^{-5}$	$5.3 \pm 2.6 \times 10^{-6}$	

Table I-3. (continued)

Element	Relative secondary ion intensity			
	Groundmass	Olivine	Groundmass	Plagioclase
$^{12}\text{C}$	$2.25 \pm 0.14 \times 10^{-5}$	$6.95 \pm 0.65 \times 10^{-5}$	$4.30 \pm 0.11 \times 10^{-5}$	$2.11 \pm 0.51 \times 10^{-5}$
$^{28}\text{Si}$	1.00	1.00	1.00	1.00
$^{29}\text{Si}$	$4.78 \times 10^{-2}$	$4.74 \times 10^{-2}$	$4.77 \times 10^{-2}$	$4.96 \times 10^{-2}$
$^{30}\text{Si}$	$3.01 \times 10^{-2}$	$2.85 \times 10^{-2}$	$3.06 \times 10^{-2}$	$3.15 \times 10^{-2}$
$^{47}\text{Ti}$	$5.44 \times 10^{-3}$	$4.9 \pm 1.4 \times 10^{-5}$	$6.23 \times 10^{-3}$	$1.15 \times 10^{-4}$
$^{74}\text{Ge}$	$2.15 \pm 0.24 \times 10^{-4}$	$2.39 \pm 0.12 \times 10^{-5}$	$2.08 \times 10^{-4}$	$8.70 \pm 0.68 \times 10^{-5}$
$^{90}\text{Zr}$	$7.22 \pm 0.62 \times 10^{-5}$	-	$9.3 \pm 1.2 \times 10^{-5}$	$3.6 \pm 1.4 \times 10^{-6}$
$^{31}\text{P}$	$1.11 \pm 0.08 \times 10^{-4}$	$3.30 \pm 0.74 \times 10^{-5}$	$1.24 \times 10^{-4}$	$8.9 \pm 1.6 \times 10^{-5}$
$^{75}\text{As}$	$1.31 \pm 0.15 \times 10^{-4}$	$2.08 \pm 0.20 \times 10^{-4}$	$1.19 \times 10^{-4}$	$3.82 \pm 0.63 \times 10^{-5}$
OH ( $^1\text{H}$ )	$5.60 \pm 0.95 \times 10^{-2}$	$1.14 \pm 0.19 \times 10^{-1}$	$7.90 \pm 0.91 \times 10^{-2}$	$5.67 \pm 0.49 \times 10^{-2}$
$^{19}\text{F}$	$6.56 \pm 0.54 \times 10^{-5}$	$1.60 \pm 0.48 \times 10^{-5}$	$9.78 \pm 0.82 \times 10^{-5}$	$2.09 \times 10^{-5}$
OH* ( $^1\text{H}$ )	$7.54 \times 10^{-1}$	1.04	$5.39 \pm 0.57 \times 10^{-1}$	$2.55 \times 10^{-1}$
$^{19}\text{F}^*$	$1.85 \times 10^{-1}$	$1.75 \pm 0.12 \times 10^{-2}$	$1.51 \times 10^{-1}$	$4.81 \times 10^{-3}$
$^{35}\text{Cl}^*$	$1.02 \pm 0.06 \times 10^{-1}$	$1.38 \pm 0.10 \times 10^{-1}$	$9.10 \times 10^{-2}$	$3.06 \pm 0.27 \times 10^{-2}$
$^{16}\text{O}$	$3.76 \times 10^{-3}$	$4.44 \times 10^{-3}$	$3.95 \times 10^{-3}$	$4.70 \times 10^{-3}$
$^{32}\text{S}$	$5.5 \pm 1.1 \times 10^{-5}$	$3.2 \pm 1.6 \times 10^{-5}$	$6.48 \pm 0.77 \times 10^{-5}$	$1.9 \pm 1.2 \times 10^{-6}$
$^{16}\text{O}^*$	$1.88 \times 10^2$	$2.30 \times 10^2$	$1.82 \times 10^2$	$9.18 \pm 0.54 \times 10^1$
$^{32}\text{S}^*$	$4.93 \pm 0.31 \times 10^{-2}$	$6.80 \pm 0.68 \times 10^{-2}$	$4.87 \times 10^{-2}$	$2.60 \pm 0.17 \times 10^{-3}$
$^{14}\text{N}$	$2.57 \pm 0.70 \times 10^{-5}$	$1.03 \pm 0.13 \times 10^{-4}$	$2.46 \pm 0.45 \times 10^{-5}$	$1.67 \pm 0.33 \times 10^{-5}$

Values determined by using secondary positive-ion detection of SIMS. (\*) Values determined by using secondary negative-ion detection of SIMS. † Standard deviation calculated from counting statistics, which is larger than 5%.

ratio:  $D = C_s / C_l$ , where  $C_s$  is the concentration of the element in the solid at a particular stage,  $C_l$  is the concentration of the elements in the melt that is in equilibrium with the solid. Ray and Hart(1982) recognized about 30%(in average) different yield for both major and trace elements between silicate glass and Ca-rich clino-pyroxene of the same composition. Such a matrix effect are probably recognized between the glass and the olivine or the plagioclase in this study. As shown in Table I-4, the relative ion intensity ratios of each major element normalized for the  $^{28}\text{Si}$  value for both olivine- and plagioclase-groundmass systems have the values corresponding to the partition coefficients measured by EPMA within a 35% error. The error value do agree with the value of the matrix effect given in Ray and Hart (1982). The relative ion intensity ratios for trace elements are also consistent with partition coefficients reported previously ( e.g., Matsui et al., 1977; Irving, 1978), the only exception being the Ni value in the olivine-groundmass system. The similar anomaly of Ni data is also reported by Ray and Hart (1982) and it may be due to Ni contamination in the primary-ion beam as discussed by them.

Therefore, we can assume, as a first approximation, that the measured relative ion intensity ratios are equivalent to the partition coefficients within about 30% error except for O, Ni and Ge data: although the verification of this assumption needs further development of quantitative techniques for SIMS. This new method is suitable for obtaining a set of coherent data for major and trace elements partitioning from the micro area in equilibrium of a given sample.

Table I-4. Partition coefficients of the elements between phenocrysts and  
groundmass

Element	Ionic radius° /pm	Partition coefficient			
		Olivine		Plagioclase	
		EPMA <sup>oo</sup>	SIMS <sup>ooo</sup>	EPMA <sup>oo</sup>	SIMS <sup>ooo</sup>
Li	76	-	$4.24 \times 10^{-1}$	-	$1.19 \times 10^{-1}$
Na	102	-	$3.79 \times 10^{-3}$	$7.46 \times 10^{-1}$	$5.24 \times 10^{-1}$
K	138	-	$2.47 \times 10^{-3}$	-	$1.23 \times 10^{-1}$
Mg	72.0	5.68	6.57	$2.95 \times 10^{-2}$	$2.46 \times 10^{-2}$
Ca	100	$2.55 \times 10^{-2}$	$3.43 \times 10^{-2}$	1.37	1.20
Mn	83	1.35	1.15	-	$1.88 \times 10^{-2}$
Fe**	78	1.43	1.37	$4.13 \times 10^{-2}$	$2.77 \times 10^{-2}$
Co	74.5	-	3.00	-	$1.83 \times 10^{-2}$
Cu	73	-	$9.29 \times 10^{-2}$	-	$5.80 \times 10^{-2}$
Zn	74.0	-	$9.26 \times 10^{-1}$	-	-
Sr	118	-	$1.06 \times 10^{-2}$	-	1.82
Cd	95	-	-	-	$7.63 \times 10^{-1}$
Ba	135	-	-	-	$2.26 \times 10^{-1}$
B	27	-	-	-	$8.20 \times 10^{-1}$
Al	53.5	-	$4.43 \times 10^{-3}$	2.07	1.69
Sc	74.5	-	$2.35 \times 10^{-1}$	-	$1.55 \times 10^{-2}$
V	64.0	-	$2.98 \times 10^{-2}$	-	$8.51 \times 10^{-3}$
Cr	61.5	-	$5.87 \times 10^{-1}$	-	$1.07 \times 10^{-2}$
Ga	62.0	-	-	-	$5.78 \times 10^{-1}$
Y	90.0	-	-	-	$2.89 \times 10^{-2}$
La	103.2	-	-	-	$1.36 \times 10^{-1}$
Ce	101	-	-	-	$9.15 \times 10^{-2}$



Table 4. (continued)

Element	Ionic radius <sup>°</sup> /pm	Partition coefficient			
		Olivine		Plagioclase	
		EPMA <sup>°°</sup>	SIMS <sup>°°°</sup>	EPMA <sup>°°</sup>	SIMS <sup>°°°</sup>
C	16	-	2.36	-	$4.49 \times 10^{-1}$
<sup>28</sup> Si	40	$7.65 \times 10^{-1}$	$7.65 \times 10^{-1}$	$9.13 \times 10^{-1}$	$9.13 \times 10^{-1}$
<sup>29</sup> Si	40	$7.65 \times 10^{-1}$	$7.59 \times 10^{-1}$	$9.13 \times 10^{-1}$	$9.49 \times 10^{-1}$
<sup>30</sup> Si	40	$7.65 \times 10^{-1}$	$7.24 \times 10^{-1}$	$9.13 \times 10^{-1}$	$9.40 \times 10^{-1}$
Ti	60.5	-	$6.88 \times 10^{-3}$	-	$1.69 \times 10^{-2}$
Zr	72	-	-	-	$3.56 \times 10^{-2}$
P	38	-	$2.21 \times 10^{-1}$	-	$6.55 \times 10^{-1}$
As	46	-	1.21	-	$2.93 \times 10^{-1}$
OH	137	-	1.56	-	$6.56 \times 10^{-1}$
F	133	-	$1.87 \times 10^{-1}$	-	$1.95 \times 10^{-1}$
OH*	137	-	1.06	-	$4.32 \times 10^{-1}$
F*	133	-	$7.24 \times 10^{-2}$	-	$2.91 \times 10^{-2}$
Cl*	181	-	1.04	-	$3.07 \times 10^{-1}$
O	140	$9.43 \times 10^{-1}$	-	1.01	-
S	184	-	$4.48 \times 10^{-2}$	-	$2.63 \times 10^{-2}$
S*	184	-	$1.06 \times 10^{-1}$	-	$4.87 \times 10^{-2}$
N	146	-	3.07	-	$6.20 \times 10^{-1}$

Values determined by using secondary positive-ion detection of SIMS.

(\*) Values determined by using secondary negative-ion detection of SIMS.

(\*\*) A part of the Fe is in the trivalent state with ionic radius of 64.5 pm.

(°) Shannon (1976). (°°) Molar ratio. (°°°) Relative ion intensity ratio normalized for <sup>28</sup>Si.

## Discussion

The results obtained in this study are shown in Figs. I-1 and I-2 as PC-IR diagrams for olivine- and plagioclase-groundmass systems respectively. Ionic radius values for six-fold coordination by Shannon (1976) were used on the diagrams except for the value of N. For the value of N, the ionic radius for four-fold coordination by Shannon (1976) was used because of the absence of six-fold value.

The olivine structure is based on hexagonal close-packed array of oxygen and can be basically described by three crystallographically-distinct sites, that is, sites for four-coordinated cations (T sites), six-coordinated cations (M sites), and anions (X sites). The basic plagioclase structure can be treated as though it has two kinds of cation sites, one for smaller Si and Al ions (T site) and the other for larger alkali or alkaline-earth ions (A site), and one kind of anion site (X site).

For both systems, the three peaks in the diagrams at the left, center, and right, obviously correspond to the T, M or A, and X sites of the crystal structures respectively.

The peaks of the X sites are displayed for -1 and -2 valent ions in Figs. I-1 and I-2, and are drawn so as to make the parabola-shaped lines as smooth as possible. The most important feature in both diagrams is that the positions of peak-tops for X sites do not coincide with positions of  $O^{2-}$ , in other words, the optimum anion size for the X site is larger than the ionic radius of  $O^{2-}$  for both olivine and plagioclase structures, assuming the peak-top positions in PC-IR diagrams represent

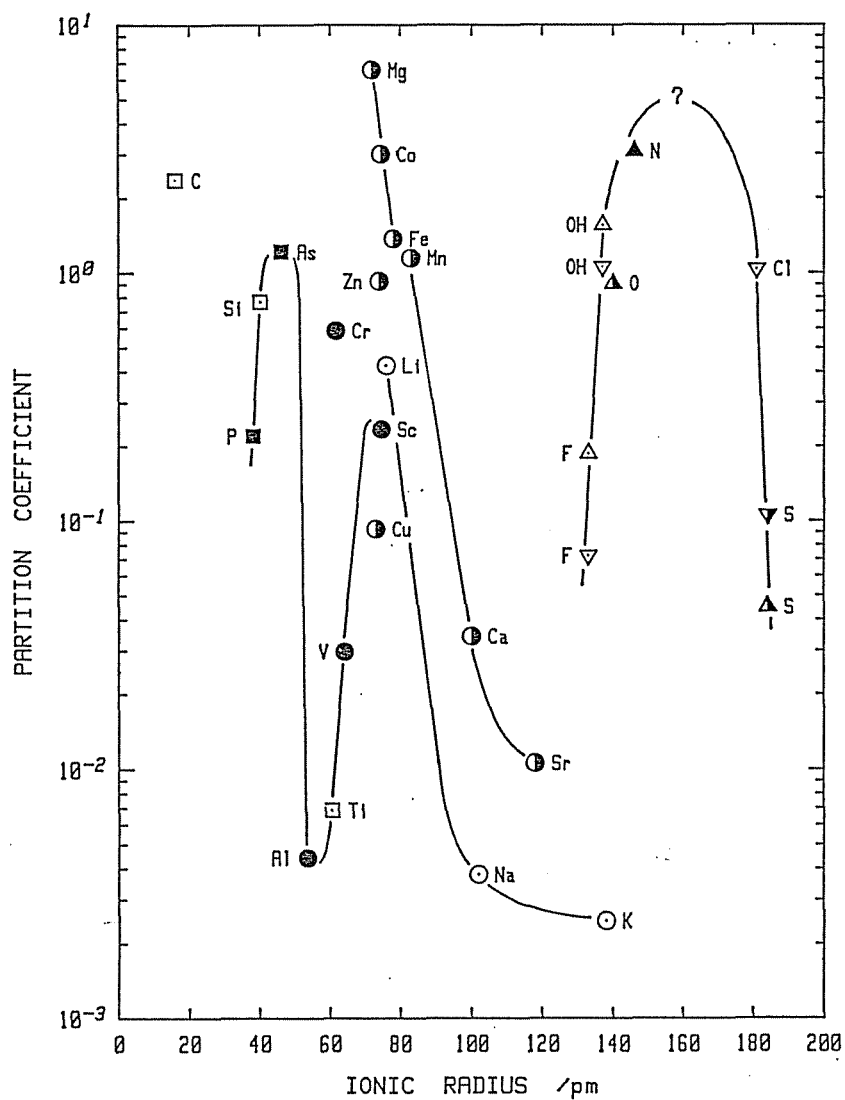


Fig. 1 Partition coefficient-ionic radius diagram for olivine-groundmass system.

⊙: +1 valent ions, ⊙: +2 valent ions, ⊙: +3 valent ions,  
 □: +4 valent ions, ■: +5 valent ions, △: -1 valent ions,  
 △: -2 valent ions, ▲: -3 valent ions.

Above ions were measured using secondary positive-ion detection of SIMS except for O ion. The partition coefficient of O was calculated from EPMA Data.

▽: -1 valent ions, ▽: -2 valent ions,

Above ions were measured using secondary negative-ion detection of SIMS.

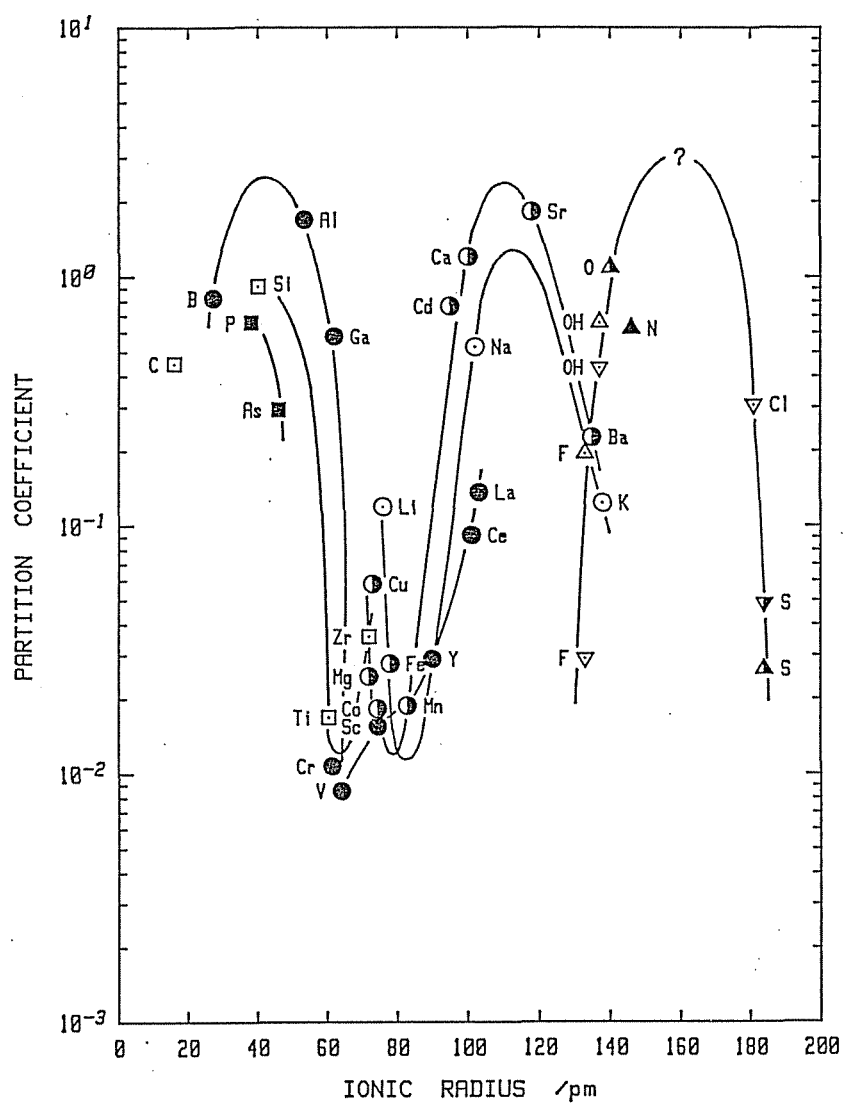


Fig. 2 Partition coefficient-ionic radius diagram for plagioclase-groundmass system. Symbols are the same as in Fig. 1.

optimum ion sizes for the crystallographic sites in the relevant mineral structure (Onuma et al., 1968).

In the olivine-groundmass system, the peaks for the M sites are very similar in shape to those reported previously (Matsui et al., 1977). Phosphorus and arsenic are substituted the T site of olivine structure (Paques-Ledent and Tarte, 1974). Silicon is the major element of the T site. The curve for Si, P, As and Al ions can be composed of one parabola for the T site, as predicted by Matsui et al. (1977), and the position of peak-top appears to be at the radius which is larger than that of Si. This observation is supported by the partition coefficient of Ge (0.5-0.7) between olivine and silicate melt (Capobianco and Watson, 1982). According to the diagram, the optimum cation for the T site in olivine has the size of  $\text{As}^{5+}$ , not  $\text{Si}^{4+}$ . The synthetic arsenate olivines were reported by Paques-Ledent and Tarte (1974): although the details of the crystal structures have not been investigated. The deviation from the smooth curve is observed in  $\text{Zn}^{2+}$ ,  $\text{Cu}^{2+}$  and  $\text{Cr}^{3+}$ . The reason for the deviations of  $\text{Zn}^{2+}$  and  $\text{Cr}^{3+}$  are due to the tetrahedral preference of Zn ion in oxide compounds and the strong crystal field stabilization energies of Cr ion (Matsui et al., 1977). The deviation of  $\text{Cu}^{2+}$  is due to the well-known square planar coordination preference of Cu ion, as exemplified by the non-existence of the  $\text{Cu}_2\text{SiO}_4$  with the olivine structure. Copper ion can be substituted only less than 2.5% in the solid solution of the silicate olivine (Schmitz-Dumont et al.).

In the plagioclase-groundmass system, it is also confirmed in this study that Ca and Na ions are a little too small to fit in A sites

(Higuchi and Nagasawa, 1969; Jensen, 1973; Matsui et al., 1977). In contrast to the olivine-groundmass system, the optimum ion for the T site has the size of  $\text{Si}^{4+}$ , and this difference is perhaps related to the corner-sharing tetrahedral framework in the feldspar structure rather than the oxygen packing mode.

We measured Fe as total Fe and plotted the partition coefficients on the basis of total Fe as  $\text{Fe}^{2+}$  in the diagram. The large discrepancy between the observed partition coefficient of Fe and the curve for divalent cations in the plagioclase-groundmass system perhaps appears to be due to the existence of Fe as  $\text{Fe}^{3+}$  in significant amount in the plagioclase.

The characteristics of partition patterns discussed above may derive the following conclusion:

- (1) Partition patterns for cations observed in this study are consistent with the result of Matsui et al. (1977).
- (2) The patterns for anions observed seem to indicate that the "crystal structure control" mechanism is applicable to anion site.

## II. PHENOCRYST/MAGMA PARTITIONING IN BONINITE

### Experimental

#### Sample

Boninite is a highly magnesian but relatively siliceous and glassy rock which containing one or more varieties of pyroxene, accessory magnesio chromite and, commonly, minor amounts of olivine. Some or all of the pyroxenes have a morphology characteristic of rapid growth. Lathes of amphibole or plagioclase microlite are rare. (Cameron et al., 1979). Kuroda and Shiraki (1975) have investigated the boninite and related rocks in the Bonine Islands and state that the boninite might have been formed by strong fractionation and quenching of partial melting product derived from the hydrous upper mantle. More detail investigations (Kuroda et al., 1978; Cameron et al., 1979, 1983; Hickey and Frey, 1983) confirmed the earlier idea and developed the geochemical models.

The boninite sample used (CJ-02) was collected from quenched-rim part of pillow lava at Tsuru-hama, Chichi-jima, Bonine Island, Japan. The rock sample consists of bronzite, augite, clinoenstatite and chrome spinel phenocrysts, dendritic to fine acicular pyroxene microlites and unaltered groundmass glass. It contains about 10 modal% phenocrysts and about 90 modal% groundmass glass.

The bronzite phenocrysts are usually euhedral to subhedral. Augite occurs as euhedral phenocrysts and as overgrowth on bronzite phenocrysts. Parallel growth of augite and bronzite phenocrysts is

sometimes observed. Clinoenstatite phenocrysts are anhedral and are rimmed or overgrown by bronzite. Clinoenstatite in chichi-jima have been described in detail by Komatsu (1980) and Shiraki et al. (1980). Chrome spinel is very rare and occurs as phenocryst and inclusion of clinoenstatite. The shape is microcube up to 0.2 mm.

I measured bronzite phenocryst partially overgrown by augite and the overgrown augite ~~on it~~ in thin section no. CJ-02A; <sup>(Fig 1 (a))</sup> bronzite and augite phenocrysts in CJ-02B; <sup>(Fig 1 (b))</sup> clinoenstatite phenocryst rimmed by epitaxial grown bronzite and the epitaxial bronzite in CJ-02C; <sup>(Fig 1 (c))</sup> chrome spinel phenocryst in CJ-02B; and the coexisting glass using EPMA and SIMS. <sup>(Fig 1 (d))</sup>

#### SIMS analysis

The SIMS instrument used in this study is the Cameca IMS-3f ion-mass microanalyzer at the Chemical Analysis Center of the University of Tsukuba. A beam of  $O^-$  ions with net energy of 13.8 keV (for secondary positive-ion detection) and 8.0 keV (for secondary negative-ion detection) was focused with a spot about 15  $\mu m$  in diameter on the gold-coated surface of a polished thin section. The vacuum of sample chamber is 0.5  $\mu Pa$ . The secondary ion intensities were measured by an electron multiplier coupled with pulse-counting circuitry with a mass resolution of about 5000 (10% valley), with the use of a cold trap of liquid nitrogen for more clean vacuum around the sample surface. Positive secondary ion intensity ratios relative to  $^{28}Si$  were measured for Li, Na, K, Mg, Ca, Mn, Fe, Co, Cu, Zn, Sr, B, Al, Sc, V, Cr, Ga, Y, C, Si, Ti, Zr, P, As, H, F, S and N. Negative secondary ion intensity ratios relative to  $^{28}Si$  were measured for H, F, Cl and S. Other experimental procedures were similar to those employs by Yurimoto and



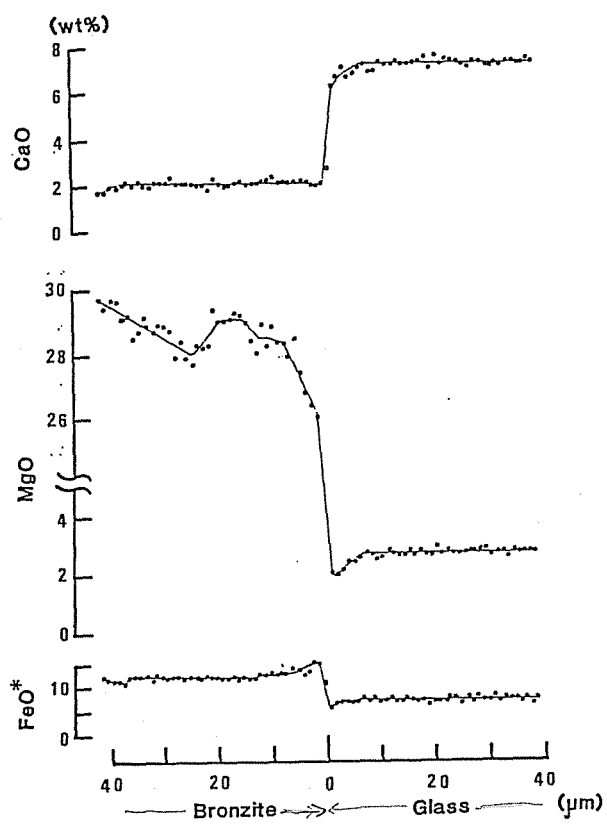
Sueno (1984a).

#### EPMA analysis

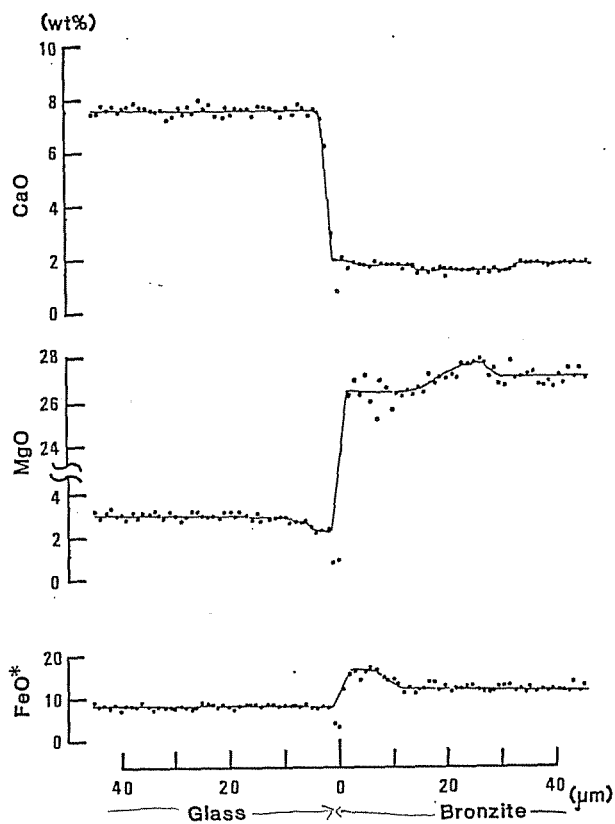
The EPMA system at the Chemical Analysis Center of the University of Tsukuba, which consists of a JXA50A (JEOL) main part and an ACPs-XR (ELIONIX) controlling part, was used with an accelerating voltage of 15 kV and a probe current of 0.016  $\mu$ A on a Faraday cage. A beam spot of about 1-2  $\mu$ m in diameter was used. The Bence and Albee (1968) method was applied to make quantitative analysis corrections. Other experimental procedures were similar to those employed by Yurimoto and Sueno (1984a).

#### Results

EPMA line analyses across the contact between bronzite phenocrysts (CJ-02A and CJ-02B) and adjacent groundmass glass are shown in Fig. II-1. At the outermost rim of bronzite, normally-zoned structure (enrichment of FeO\* content and the depletion of MgO content) is observed. The composition of glass are also modified at the contact with bronzite. These compositional zonings suggest that the growth of the bronzite phenocrysts were continued just before solidification of the magma and physicochemical conditions change rapidly at the last stage of the magmatism. The zoning of the bronzite at the outermost rim and <sup>of</sup> the glass at the contact may be formed during the eruption and quenching of the magma. It is considered that the bulk liquid composition was little affected by the event of the <sup>(eruption and quenching)</sup> last stage because a large proportion of the rock is occupied by the glass and the zoning of glass can be observed only at the contact with crystals. Therefore, the bulk liquid composition is equilibrated with the rim of the bronzite phenocryst except for the outermost rim part.



(A)



(B)

Fig. II-1 Electron microprobe traces across contact between  
bronzite and glass. (A) CJ-02A, (B) CJ-02B

EPMA line traverse analysis of clinoenstatite (CJ-02C) and glass are shown in Fig. II-2. It is widely accepted that clinoenstatite in nature was originally protoenstatite which inverted to clinoenstatite upon cooling. The inverted protoenstatite is rimmed by epitaxial bronzite. The epitaxial bronzite have normally-zoned structure at the outermost rim similar to the bronzite phenocrysts as shown in Fig. II-1. There is a crack or small void at the boundary between the overgrown bronzite and the glass. The relationship between the epitaxial bronzite and groundmass glass may be the same as the relationship between the bronzite phenocrysts and the glass although the compositional zoning in glass can not be observed because of the crack. Therefore, it is considered that the bulk liquid composition is equilibrated with the epitaxial bronzite except for the outermost rim part. The protoenstatite, which is an original form of the clinoenstatite, has been crystalized from the magma at the earlier stage. The protoenstatite is not equilibrated with the bulk liquid composition because the inverted protoenstatite is not in contact directly with the groundmass glass. However, obvious compositional zoning can not be observed in the inverted protoenstatite. The volume of the epitaxial bronzite is very small <sup>(about less than 10 um thick)</sup> when it is compared with the volume of the groundmass glass. Therefore, the chemical change of the liquid composition may have been very small during crystalization of the overgrown bronzite. We <sup>can</sup> assume that the protoenstatite is nearly equilibrated with the bulk liquid composition.

EPMA line analyses across the contact between overgrown augite on bronzite phenocryst (CJ-02A), augite phenocryst (CJ-02B) and the adjacent groundmass glass are shown in Fig. II-3. The composition of

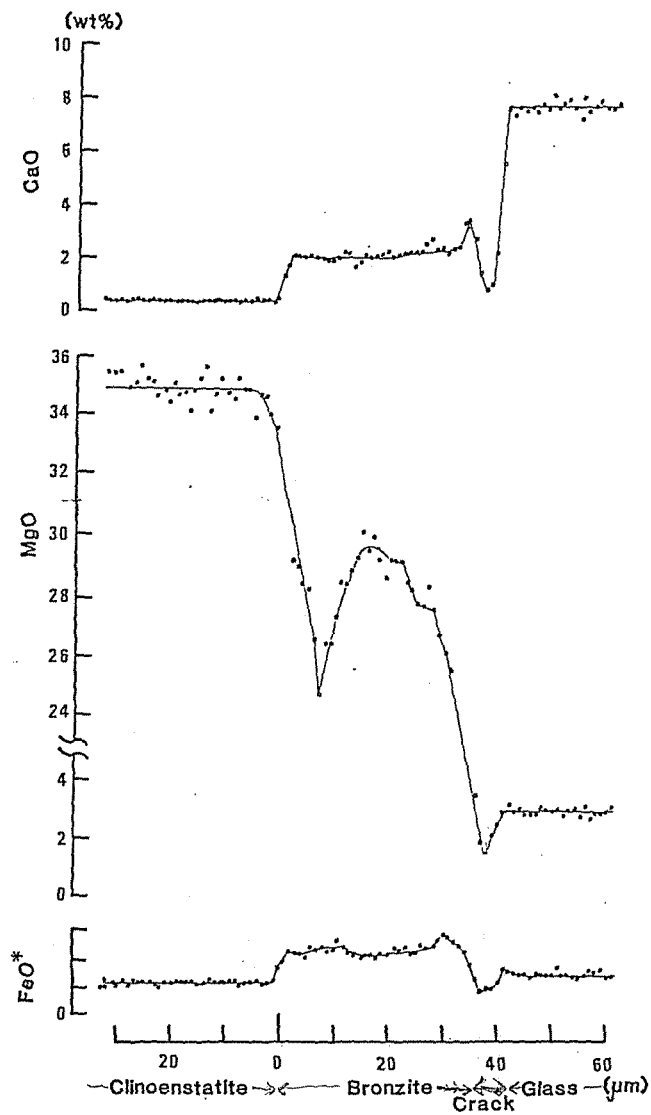
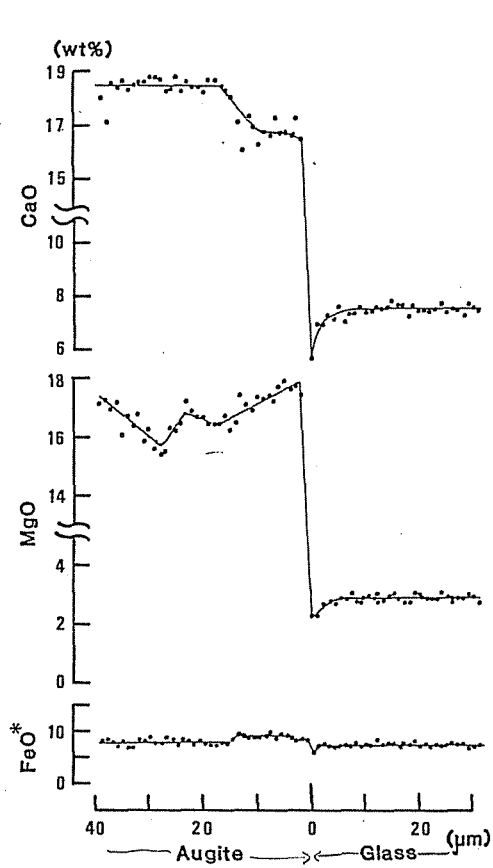


Fig. II-2 Electron microprobe traces across contacts among clinoenstatite, epitaxial bronzite and glass.

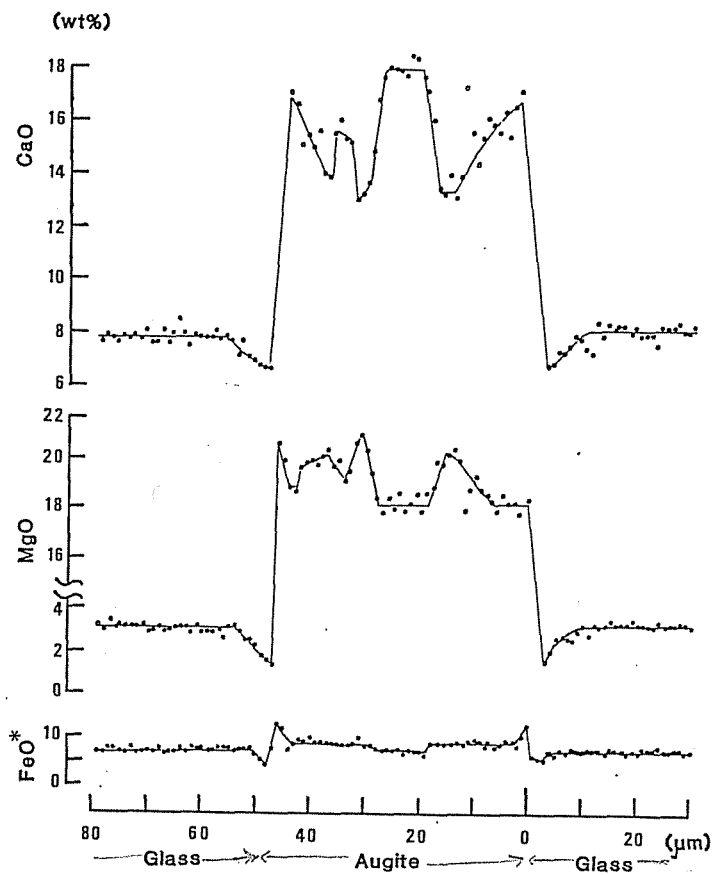
glass are modified at the contact with augite. At the outermost rim of the overgrown augite ~~on-bronzite~~ (CJ-02A), compositional zoning structure which is enrichment of MgO' and FeO\* content and depletion of CaO content, is observed (Fig. II-3A), while complex zoning structure is observed in the augite phenocryst (CJ-02B, Fig. II-3B). The chemical composition of the outermost rim of both augites have similar values. These evidences suggest that the growth of the outermost rim of the augite might have been formed during the eruption and quenching of the magma (similar to the results obtained from the outermost rim on the bronzite <sup>like</sup> phenocryst. ~~The bulk liquid have not been achieved in equilibrium with the outermost rims of augite.~~ Therefore it is considered that the bulk liquid composition is equilibrated with the rim of the overgrown augite, excluding the outermost rim part and the core part of the augite phenocryst.

EPMA line analyses across the contact between chrome spinel phenocryst (CJ-02C) and adjacent groundmass glass are shown in Fig. II-4. Normally-zoned structure is observed in the chrome spinel phenocryst. At the outermost rim of the chrome spinel, abrupt increase of FeO\* content and decrease of MgO and Al<sub>2</sub>O<sub>3</sub> contents are detected. In the glass part, Alumina content is modified at the contact with the chrome spinel but the other compositions did not show any clear gradients on EPMA line analysis. These compositional zonings on both sides of the contact suggest that the bulk liquid composition is equilibrated with the rim of the chrome spinel except for the outermost rim part.

The bulk liquid compositions equilibrated with each mineral were measured with EPMA and SIMS by analyzing the homogenous area near each



(A)



(B)

Fig. II-3 Electron microprobe traces across contact between augite and glass. (A) CJ-02A, (B) CJ-02B

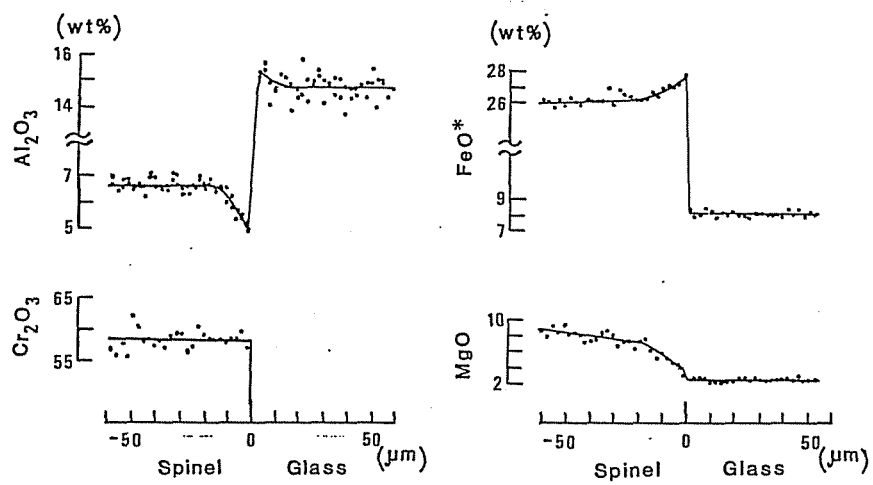


Fig. II-4      Electron microprobe traces across contact between spinel and glass.

mineral. Each mineral composition equilibrated with the bulk liquid composition were also measured with EPMA and SIMS by analyzing the rim of the mineral except for the outermost rim. EPMA and SIMS results are listed in Tables II-1 and II-2, respectively. It is considered the analyzed minerals and glass is about in equilibrium one another because the chemical compositions of each glass have essentially the equivalent values as shown in Table II-1.

Partition coefficient values calculated from the values in Tables II-1 and II-2 are listed in Table II-3. The partition coefficient  $D(i)$  of a particular element  $i$  is defined as the ratio:  $D(i) = C_i^S / C_i^L$ , where  $C_i^S$  is the concentration of the element  $i$  in the solid phase at a particular stage,  $C_i^L$  is the concentration of the element  $i$  in the liquid phase that is in equilibrium with the solid.

Ray and Hart (1982) recognized about 30% (in average) different yield of secondary ion for both major and trace elements between silicate glass and Ca-rich clinopyroxene. Such a matrix effect is probably recognized between the solid and liquid in this study. However, Yurimoto and Sueno (1984a) found that relative ion intensity ratios normalized for the  $^{28}\text{Si}$  value for olivine- and plagioclase-groundmass glass systems had the values corresponding to the partition coefficients. The relative ion intensity ratios normalized for  $^{28}\text{Si}$  between phenocrysts and the groundmass glasses as well as between augites and bronzites are plotted in Fig. II-5 against partition coefficients calculated by EPMA analyses. In the spinel-groundmass glass system, the relative ion intensity ratios were normalized for the  $^{27}\text{Al}$  instead of  $^{28}\text{Si}$  because Si concentration in the spinel was under



Table II-1 Electron microprobe analyses of phenocrysts and the coexisting groundmass glass in boninite

	CJ-02B		CJ-02A			CJ-02B			CJ-02C		
	Spinel	Glass	OG-Aug	Brz	Glass	Aug	Brz	Glass	Clino-En	OG-Brz	Glass
SiO <sub>2</sub>	-	61.76±0.69	52.76±0.30	55.34±0.48	62.26±0.50	53.41±0.48	55.38±0.56	62.09±1.03	57.52±0.46	55.16±0.69	61.33±0.41
TiO <sub>2</sub>	-	0.24±0.03	0.09±0.02	-	0.25±0.02	0.10±0.02	-	0.26±0.03	-	-	0.24±0.03
Al <sub>2</sub> O <sub>3</sub>	6.89±0.32	14.63±0.28	2.36±0.16	0.63±0.07	14.56±0.23	1.78±0.29	1.41±0.10	14.52±0.48	0.46±0.19	1.18±0.26	15.03±0.15
Cr <sub>2</sub> O <sub>3</sub>	59.06±1.31	-	-	-	-	0.46±0.16	-	-	0.32±0.13	0.29±0.04	-
FeO*	25.61±1.13	7.88±0.44	8.72±0.25	11.84±1.10	7.90±0.18	8.89±0.55	11.93±0.14	7.79±0.30	6.40±0.32	11.80±0.45	7.71±0.39
MnO	0.38±0.07	0.21±0.04	0.30±0.02	0.42±0.04	0.20±0.04	0.23±0.08	0.29±0.05	0.17±0.04	0.23±0.07	0.32±0.05	0.17±0.04
MgO	8.20±0.85	3.04±0.11	16.74±0.42	28.60±0.85	2.84±0.11	18.55±0.60	27.81±0.38	2.87±0.21	34.86±0.84	29.24±0.32	3.14±0.21
CaO	-	7.55±0.17	18.67±0.70	2.03±0.16	7.46±0.09	16.29±1.07	2.55±0.27	7.56±0.27	0.34±0.03	2.03±0.14	7.83±0.21
Na <sub>2</sub> O	-	2.04±0.26	0.19±0.02	-	2.04±0.32	0.18±0.02	-	2.12±0.23	-	-	1.97±0.31
K <sub>2</sub> O	-	0.54±0.02	-	-	0.55±0.05	-	-	0.55±0.03	-	-	0.53±0.04
Total	100.14	97.89	99.83	98.86	98.06	99.89	99.45	97.93	100.13	100.02	97.95

Spinel = chrome spinel phenocryst, Glass = groundmass glass, OG-Aug = Overgrown augite on bronzite, Brz = Bronzitem phenocryst, Aug = augite phenocryst, Clino-En = inverted protoenstatite phenocryst, OG-Brz = epitaxial grown bronzite on Proto-En. \* total iron as FeO.

Table II-2 Relative ion intensities of SIMS analyses for exsolution and the host pyroxenes

Element	CJ-02B Relative secondary ion intensity				CJ-02A	
	Spinel	Glass	OG-Aug	Brz	Glass	
<sup>7</sup> Li	6.81±0.09 <sup>b</sup> ×10 <sup>-1</sup>	9.44 ×10 <sup>-4</sup>	3.26±0.46 ×10 <sup>-4</sup>	2.70±0.53 ×10 <sup>-4</sup>	1.33±0.41 ×10 <sup>3</sup>	
<sup>23</sup> Na	4.76 ×10 <sup>-1</sup>	1.14 ×10 <sup>0</sup>	9.70±0.24 ×10 <sup>-2</sup>	1.65 ×10 <sup>-2</sup>	1.33±0.19 ×10 <sup>0</sup>	
<sup>39</sup> K	1.41±0.09 ×10 <sup>-1</sup>	3.82 ×10 <sup>-1</sup>	7.70±0.61 ×10 <sup>-4</sup>	1.32±0.70 ×10 <sup>-4</sup>	3.92±0.59 ×10 <sup>-1</sup>	
<sup>26</sup> Mg	6.55 ×10 <sup>2</sup>	3.67 ×10 <sup>-2</sup>	3.39±0.25 ×10 <sup>-1</sup>	5.07±0.87 ×10 <sup>-1</sup>	4.41±0.27 ×10 <sup>-2</sup>	
<sup>40</sup> Ca	1.56±0.09 ×10 <sup>0</sup>	1.22 ×10 <sup>0</sup>	5.07±0.36 ×10 <sup>0</sup>	4.45±0.55 ×10 <sup>-1</sup>	1.31±0.10 ×10 <sup>0</sup>	
<sup>55</sup> Mn	8.36 ×10 <sup>1</sup>	6.85 ×10 <sup>-3</sup>	1.59±0.23 ×10 <sup>-2</sup>	2.00 ×10 <sup>-2</sup>	7.62 ×10 <sup>-3</sup>	
<sup>56</sup> Fe	3.41±0.17 ×10 <sup>3</sup>	2.94 ×10 <sup>-1</sup>	3.60±0.71 ×10 <sup>-1</sup>	5.19±0.47 ×10 <sup>-1</sup>	3.07 ×10 <sup>-1</sup>	
<sup>59</sup> Co	3.49±0.40 ×10 <sup>0</sup>	1.08 ×10 <sup>-4</sup>	2.68±0.62 ×10 <sup>-4</sup>	4.99±0.34 ×10 <sup>-4</sup>	1.08±0.08 ×10 <sup>-4</sup>	
<sup>63</sup> Cu	5.19±0.54 ×10 <sup>-2</sup>	1.53 ×10 <sup>-4</sup>	1.11±0.10 ×10 <sup>-5</sup>	6.97±0.35 ×10 <sup>-6</sup>	1.43±0.09 ×10 <sup>-4</sup>	
<sup>66</sup> Zn	7.96±0.70 ×10 <sup>-2</sup>	1.28 ×10 <sup>-5</sup>	8.04±1.51 ×10 <sup>-6</sup>	1.72±0.24 ×10 <sup>-5</sup>	8.75±0.78 ×10 <sup>-6</sup>	
<sup>88</sup> Sr	5.33±1.40 ×10 <sup>-3</sup>	7.67 ×10 <sup>-4</sup>	7.55±0.86 ×10 <sup>-5</sup>	1.05 ×10 <sup>-5</sup>	7.82±0.65 ×10 <sup>-4</sup>	
<sup>11</sup> B	5.79±0.21 ×10 <sup>-3</sup>	9.72±0.58 ×10 <sup>-5</sup>	1.65±0.08 ×10 <sup>-5</sup>	1.91±0.56 ×10 <sup>-5</sup>	1.09±0.07 ×10 <sup>-4</sup>	
<sup>27</sup> Al	7.50 ×10 <sup>3</sup>	1.18 ×10 <sup>0</sup>	2.61 ×10 <sup>-1</sup>	1.09±0.35 ×10 <sup>-1</sup>	1.28±0.15 ×10 <sup>0</sup>	
<sup>45</sup> Sc	1.05 ×10 <sup>0</sup>	3.63 ×10 <sup>-4</sup>	2.46 ×10 <sup>-3</sup>	4.93±0.67 ×10 <sup>-4</sup>	4.75±0.65 ×10 <sup>-4</sup>	
<sup>51</sup> V	6.08 ×10 <sup>1</sup>	1.54 ×10 <sup>-3</sup>	1.99±0.18 ×10 <sup>-3</sup>	4.23±1.25 ×10 <sup>-4</sup>	1.94±0.25 ×10 <sup>-3</sup>	
<sup>52</sup> Cr	2.11 ×10 <sup>4</sup>	7.55±0.80 ×10 <sup>-5</sup>	8.11±0.63 ×10 <sup>-3</sup>	7.80±1.50 ×10 <sup>-3</sup>	4.49±0.37 ×10 <sup>-5</sup>	
<sup>69</sup> Ga	9.03 ×10 <sup>-1</sup>	4.50 ×10 <sup>-5</sup>	1.74 ×10 <sup>-5</sup>	7.43±0.74 ×10 <sup>-6</sup>	4.52±0.13 ×10 <sup>-5</sup>	
<sup>89</sup> Y	-	2.63 ×10 <sup>-5</sup>	2.88±0.40 ×10 <sup>-5</sup>	4.45±0.47 ×10 <sup>-6</sup>	3.27±0.52 ×10 <sup>-5</sup>	
<sup>12</sup> C	-	2.16 ×10 <sup>-6</sup>	8.19±0.81 ×10 <sup>-6</sup>	-	2.76 ×10 <sup>-6</sup>	
<sup>28</sup> Si	1.00	1.00	1.00	1.00	1.00	
<sup>29</sup> Si	4.33 ×10 <sup>-2</sup>	5.29 ×10 <sup>-2</sup>	5.08 ×10 <sup>-2</sup>	5.11 ×10 <sup>-2</sup>	5.11 ×10 <sup>-2</sup>	
<sup>30</sup> Si	3.78 ×10 <sup>-2</sup>	3.31 ×10 <sup>-2</sup>	3.33 ×10 <sup>-2</sup>	3.13 ×10 <sup>-2</sup>	3.29 ×10 <sup>-2</sup>	
<sup>47</sup> Ti	3.67±0.20 ×10 <sup>0</sup>	9.02 ×10 <sup>-4</sup>	4.17 ×10 <sup>-4</sup>	1.22±0.14 ×10 <sup>-4</sup>	1.09±0.16 ×10 <sup>-3</sup>	
<sup>90</sup> Zr	-	3.70 ×10 <sup>-5</sup>	-	-	3.81 ×10 <sup>-5</sup>	
<sup>31</sup> P	-	5.46 ×10 <sup>-5</sup>	1.76±0.66 ×10 <sup>-5</sup>	2.55±0.53 ×10 <sup>-5</sup>	5.88 ×10 <sup>-5</sup>	
<sup>75</sup> As	2.22±0.26 ×10 <sup>-1</sup>	4.33 ×10 <sup>-4</sup>	3.51±0.27 ×10 <sup>-5</sup>	1.49±0.30 ×10 <sup>-4</sup>	8.55 ×10 <sup>-4</sup>	
OH ( <sup>1</sup> H)	1.61±0.16 ×10 <sup>1</sup>	1.38 ×10 <sup>-2</sup>	4.96±0.46 ×10 <sup>-3</sup>	6.46±1.00 ×10 <sup>-3</sup>	1.28±0.09 ×10 <sup>-3</sup>	
<sup>19</sup> F	1.07±0.34 ×10 <sup>-2</sup>	3.58 ×10 <sup>-5</sup>	2.02±0.18 ×10 <sup>-5</sup>	1.45±0.37 ×10 <sup>-5</sup>	4.30±0.79 ×10 <sup>-5</sup>	
OH <sup>a</sup> ( <sup>1</sup> H)	3.39 ×10 <sup>-2c</sup>	4.21±0.43 ×10 <sup>-3c</sup>	2.34 ×10 <sup>0a</sup>	1.38±0.13 ×10 <sup>0</sup>	2.45 ×10 <sup>0</sup>	
<sup>19</sup> F <sup>a</sup>	8.47 ×10 <sup>-4c</sup>	7.67±1.76 ×10 <sup>-4c</sup>	5.50±0.55 ×10 <sup>-2</sup>	9.18 ×10 <sup>-3</sup>	4.58 ×10 <sup>-1</sup>	
<sup>35</sup> Cl <sup>a</sup>	8.25±0.47 ×10 <sup>-3c</sup>	4.03±0.76 ×10 <sup>-3c</sup>	2.22±0.21 ×10 <sup>-1</sup>	1.92±0.11 ×10 <sup>-2</sup>	2.85 ×10 <sup>0</sup>	
<sup>32</sup> S	-	1.31±0.09 ×10 <sup>-5</sup>	1.70±0.17 ×10 <sup>-4</sup>	3.31±0.33 ×10 <sup>-5</sup>	1.33±0.15 ×10 <sup>-5</sup>	
<sup>32</sup> S <sup>a</sup>	2.31±0.31 ×10 <sup>-4c</sup>	2.09±0.21 ×10 <sup>-5c</sup>	1.04±0.21 ×10 <sup>-2</sup>	1.90±0.16 ×10 <sup>-3</sup>	1.30±0.17 ×10 <sup>-2</sup>	
<sup>14</sup> N	2.41 ×10 <sup>-1</sup>	3.89 ×10 <sup>-5</sup>	2.41±0.48 ×10 <sup>-5</sup>	1.70±0.13 ×10 <sup>-5</sup>	2.51±0.37 ×10 <sup>-5</sup>	

Values determined by using secondary positive-ion detection of SIMS.

<sup>a</sup> Values determined by using secondary negative-ion detection of SIMS.<sup>b</sup> Standard deviation calculated from counting statistics, which is larger than 5%.<sup>c</sup> normalized for <sup>16</sup>O.

1.07 × 10<sup>-2</sup>  
3.58 × 10<sup>-5</sup>

Table II-2 (continued)

Element	Relative secondary ion intensity					
	CJ-02B			CJ-02C		
	Aug	Brz	Glass	Clino-En	OG-brz	Glass
<sup>7</sup> Li	3.72±0.15 <sup>b</sup> ×10 <sup>-4</sup>	2.23±0.15 ×10 <sup>-4</sup>	1.12±0.10 ×10 <sup>-3</sup>	1.44±0.11 ×10 <sup>-4</sup>	3.59 ×10 <sup>-4</sup>	7.46±0.51 ×10 <sup>-4</sup>
<sup>23</sup> Na	1.46±0.35 ×10 <sup>-1</sup>	1.69 ×10 <sup>-2</sup>	1.41 ×10 <sup>0</sup>	1.46±0.29 ×10 <sup>-3</sup>	8.86±1.09 ×10 <sup>-3</sup>	6.10±0.56 ×10 <sup>-1</sup>
<sup>39</sup> K	1.63±0.83 ×10 <sup>-3</sup>	2.85±0.21 ×10 <sup>-4</sup>	3.86 ×10 <sup>-1</sup>	5.15±2.07 ×10 <sup>-4</sup>	1.63±0.81 ×10 <sup>-3</sup>	9.51±1.44 ×10 <sup>-2</sup>
<sup>26</sup> Mg	3.75±0.45 ×10 <sup>-1</sup>	5.04 ×10 <sup>-1</sup>	4.41 ×10 <sup>-2</sup>	4.03 ×10 <sup>-1</sup>	4.16±0.37 ×10 <sup>-1</sup>	3.42 ×10 <sup>-2</sup>
<sup>40</sup> Ca	4.56±0.37 ×10 <sup>0</sup>	5.05 ×10 <sup>-1</sup>	1.37 ×10 <sup>0</sup>	5.62 ×10 <sup>-2</sup>	3.08±0.64 ×10 <sup>-1</sup>	9.30 ×10 <sup>-1</sup>
<sup>55</sup> Mn	1.91±0.15 ×10 <sup>-2</sup>	2.01±0.29 ×10 <sup>-2</sup>	8.78±0.60 ×10 <sup>-3</sup>	7.55 ×10 <sup>-3</sup>	1.19±0.38 ×10 <sup>-2</sup>	5.71 ×10 <sup>-3</sup>
<sup>56</sup> Fe	4.60±0.36 ×10 <sup>-1</sup>	5.67±0.63 ×10 <sup>-1</sup>	3.57 ×10 <sup>-1</sup>	2.07 ×10 <sup>-1</sup>	3.44±1.00 ×10 <sup>-1</sup>	2.48 ×10 <sup>-1</sup>
<sup>59</sup> Co	3.56±0.33 ×10 <sup>-4</sup>	5.34±0.39 ×10 <sup>-4</sup>	1.33 ×10 <sup>-4</sup>	2.22 ×10 <sup>-4</sup>	3.08±0.93 ×10 <sup>-4</sup>	8.57±0.50 ×10 <sup>-5</sup>
<sup>63</sup> Cu	1.26±0.11 ×10 <sup>-5</sup>	7.22±0.43 ×10 <sup>-6</sup>	1.77±0.20 ×10 <sup>-4</sup>	3.11 ×10 <sup>-6</sup>	6.45±0.56 ×10 <sup>-6</sup>	1.03 ×10 <sup>-4</sup>
<sup>66</sup> Zn	6.49±1.57 ×10 <sup>-6</sup>	1.58±0.42 ×10 <sup>-5</sup>	1.06±0.17 ×10 <sup>-5</sup>	4.30 ×10 <sup>-6</sup>	1.01±0.67 ×10 <sup>-5</sup>	1.10±0.26 ×10 <sup>-5</sup>
<sup>88</sup> Sr	6.34±0.86 ×10 <sup>-5</sup>	1.07±0.33 ×10 <sup>-5</sup>	7.83±0.61 ×10 <sup>-4</sup>	3.28±0.38 ×10 <sup>-6</sup>	2.75±0.65 ×10 <sup>-5</sup>	6.23±1.91 ×10 <sup>-4</sup>
<sup>11</sup> B	1.19±0.33 ×10 <sup>-5</sup>	4.58±0.35 ×10 <sup>-6</sup>	9.45 ×10 <sup>-5</sup>	8.58±0.49 ×10 <sup>-6</sup>	8.56±0.63 ×10 <sup>-6</sup>	9.29 ×10 <sup>-5</sup>
<sup>27</sup> Al	2.70 ×10 <sup>-1</sup>	1.44±0.08 ×10 <sup>-1</sup>	1.29 ×10 <sup>0</sup>	2.69 ×10 <sup>-2</sup>	1.04±0.17 ×10 <sup>-1</sup>	1.08 ×10 <sup>0</sup>
<sup>45</sup> Sc	2.37 ×10 <sup>-3</sup>	7.70±0.67 ×10 <sup>-4</sup>	4.21 ×10 <sup>-4</sup>	1.31 ×10 <sup>-4</sup>	3.21±1.13 ×10 <sup>-4</sup>	3.25 ×10 <sup>-4</sup>
<sup>51</sup> V	1.74±0.29 ×10 <sup>-3</sup>	6.77 ×10 <sup>-4</sup>	1.96±0.26 ×10 <sup>-3</sup>	1.43 ×10 <sup>-4</sup>	3.70±0.72 ×10 <sup>-4</sup>	1.43±0.08 ×10 <sup>-3</sup>
<sup>52</sup> Cr	2.91±0.63 ×10 <sup>-2</sup>	1.96±0.10 ×10 <sup>-2</sup>	3.58±0.32 ×10 <sup>-5</sup>	9.91 ×10 <sup>-3</sup>	1.00±0.09 ×10 <sup>-2</sup>	6.44±0.44 ×10 <sup>-5</sup>
<sup>69</sup> Ga	1.70 ×10 <sup>-5</sup>	2.39±0.54 ×10 <sup>-5</sup>	5.12±0.55 ×10 <sup>-5</sup>	-	-	2.75±0.26 ×10 <sup>-5</sup>
<sup>89</sup> Y	2.31±0.35 ×10 <sup>-5</sup>	3.13±1.32 ×10 <sup>-6</sup>	3.07±0.52 ×10 <sup>-5</sup>	1.82±0.41 ×10 <sup>-7</sup>	2.98±0.58 ×10 <sup>-6</sup>	2.15 ×10 <sup>-5</sup>
<sup>12</sup> C	5.62±1.82 ×10 <sup>-6</sup>	5.48±1.29 ×10 <sup>-6</sup>	1.19±1.43 ×10 <sup>-6</sup>	7.09±4.39 ×10 <sup>-6</sup>	8.19±3.69 ×10 <sup>-6</sup>	1.49±0.64 ×10 <sup>-5</sup>
<sup>28</sup> Si	1.00	1.00	1.00	1.00	1.00	1.00
<sup>29</sup> Si	5.16 ×10 <sup>-2</sup>	5.07 ×10 <sup>-2</sup>	5.29 ×10 <sup>-2</sup>	5.05 ×10 <sup>-2</sup>	5.06 ×10 <sup>-2</sup>	5.19 ×10 <sup>-2</sup>
<sup>30</sup> Si	3.19 ×10 <sup>-2</sup>	3.22 ×10 <sup>-2</sup>	3.32 ×10 <sup>-2</sup>	3.19 ×10 <sup>-2</sup>	3.24 ×10 <sup>-2</sup>	3.29 ×10 <sup>-2</sup>
<sup>47</sup> Ti	4.02±0.71 ×10 <sup>-4</sup>	1.60±0.13 ×10 <sup>-4</sup>	1.06±0.07 ×10 <sup>-3</sup>	1.62 ×10 <sup>-5</sup>	1.02±0.16 ×10 <sup>-4</sup>	7.43 ×10 <sup>-4</sup>
<sup>90</sup> Zr	-	-	3.28±0.28 ×10 <sup>-5</sup>	3.36±1.00 ×10 <sup>-5</sup>	-	2.69±0.59 ×10 <sup>-5</sup>
<sup>31</sup> P	8.22±1.64 ×10 <sup>-6</sup>	1.98±0.42 ×10 <sup>-6</sup>	5.62±0.62 ×10 <sup>-5</sup>	-	2.94±0.42 ×10 <sup>-6</sup>	4.26±0.40 ×10 <sup>-5</sup>
<sup>75</sup> As	3.51±0.64 ×10 <sup>-5</sup>	1.57±0.28 ×10 <sup>-5</sup>	5.65±1.43 ×10 <sup>-4</sup>	3.68 ×10 <sup>-6</sup>	9.47±0.85 ×10 <sup>-6</sup>	1.28±0.85 ×10 <sup>-4</sup>
OH ( <sup>1</sup> H)	4.96±0.46 ×10 <sup>-3</sup>	4.56±1.97 ×10 <sup>-3</sup>	1.24±0.09 ×10 <sup>-2</sup>	3.40±1.76 ×10 <sup>-3</sup>	1.38±0.12 ×10 <sup>-3</sup>	5.04±0.56 ×10 <sup>-3</sup>
<sup>19</sup> F	1.23±0.47 ×10 <sup>-5</sup>	1.07±0.38 ×10 <sup>-5</sup>	4.59±0.38 ×10 <sup>-5</sup>	5.22±2.41 ×10 <sup>-6</sup>	7.50±2.57 ×10 <sup>-6</sup>	2.63 ×10 <sup>-5</sup>
OH <sup>a</sup> ( <sup>1</sup> H)	7.00±0.38 ×10 <sup>-1</sup>	1.59 ×10 <sup>0</sup>	8.84±0.36 ×10 <sup>-1</sup>	8.49 ×10 <sup>-1</sup>	9.68±0.54 ×10 <sup>-1</sup>	9.90 ×10 <sup>-1</sup>
<sup>19</sup> F <sup>a</sup>	3.04±0.16 ×10 <sup>-2</sup>	5.01±0.44 ×10 <sup>-2</sup>	2.26±0.14 ×10 <sup>-1</sup>	1.13 ×10 <sup>-2</sup>	3.75±0.65 ×10 <sup>-2</sup>	6.95 ×10 <sup>-2</sup>
<sup>35</sup> Cl <sup>a</sup>	1.45 ×10 <sup>-1</sup>	3.47 ×10 <sup>-1</sup>	1.23 ×10 <sup>0</sup>	1.79±0.11 ×10 <sup>-2</sup>	9.18±0.65 ×10 <sup>-2</sup>	2.72 ×10 <sup>-1</sup>
<sup>32</sup> S	1.56±0.10 ×10 <sup>-4</sup>	3.64±0.41 ×10 <sup>-5</sup>	1.40±0.32 ×10 <sup>-5</sup>	3.63±0.43 ×10 <sup>-6</sup>	1.95±0.26 ×10 <sup>-5</sup>	9.25±0.49 ×10 <sup>-6</sup>
<sup>32</sup> S <sup>a</sup>	2.29±0.23 ×10 <sup>-3</sup>	1.11±0.13 ×10 <sup>-2</sup>	6.42 ×10 <sup>-3</sup>	2.38±0.67 ×10 <sup>-3</sup>	4.08±0.82 ×10 <sup>-2</sup>	7.40±1.70 ×10 <sup>-3</sup>
<sup>14</sup> N	-	1.77±0.74 ×10 <sup>-6</sup>	2.98±0.22 ×10 <sup>-5</sup>	1.95 ×10 <sup>-7</sup>	2.85 ×10 <sup>-6</sup>	9.98±1.42 ×10 <sup>-7</sup>

Values determined by using secondary positive-ion detection of SIMS.

<sup>a</sup> Values determined by using secondary negative-ion detection of SIMS.<sup>b</sup> Standard deviation calculated from counting statistics, which is larger than 5%.<sup>c</sup> normalized for <sup>16</sup>O.

Table II-3. Partition coefficients of the elements between phenocrysts and groundmass

Element	Ionic radius <sup>c</sup> /pm	Partition coefficient															
		CJ-02B		CJ-02A						CJ-02B				CJ-02C			
		Spinel		QG-Aug		Brz		Aug		Brz		Clino-En		OG-Brz		EPMA <sup>d</sup>	SIMS <sup>e</sup>
		EPMA <sup>d</sup>	SIMS <sup>e</sup>	EPMA <sup>d</sup>	SIMS <sup>e</sup>	EPMA <sup>d</sup>	SIMS <sup>e</sup>	EPMA <sup>d</sup>	SIMS <sup>e</sup>	EPMA <sup>d</sup>	SIMS <sup>e</sup>	EPMA <sup>d</sup>	SIMS <sup>e</sup>	EPMA <sup>d</sup>	SIMS <sup>e</sup>		
Li	76	-	0.0716	-	0.211	-	0.179	-	0.288	-	0.175	-	0.171	-	0.303	-	-
Na	102	-	0.0000415	0.0972	0.0628	-	0.0109	0.0867	0.0899	-	0.0105	-	0.00213	-	0.0110	-	-
K	138	-	0.0000366	-	0.00169	-	0.000296	-	0.00367	-	0.000648	-	0.00481	-	0.0105	-	-
Mg	72.0	3.61	1.77	5.98	6.62	9.96	10.1	6.50	7.38	9.51	10.0	10.5	10.4	9.11	10.9	-	-
Ca	100	-	0.000127	2.54	3.33	0.269	0.299	2.17	2.89	0.332	0.324	0.0426	0.0537	0.252	0.279	-	-
Mn <sub>b</sub>	83	2.67	1.21	1.50	1.80	2.17	2.31	1.40	1.89	1.80	2.01	1.40	1.17	2.00	1.70	-	-
Fe <sub>b</sub>	78	4.35	1.15	1.12	1.01	1.48	1.49	1.15	1.12	1.51	1.39	0.783	0.742	1.49	1.28	-	-
Co	74.5	-	3.21	-	2.14	-	4.07	-	2.32	-	3.53	-	2.30	-	3.35	-	-
Cu	73	-	0.0337	-	0.0668	-	0.0429	-	0.0618	-	0.0358	-	0.0267	-	0.0540	-	-
Zn	74.0	-	0.617	-	0.791	-	1.73	-	0.531	-	1.31	-	0.346	-	1.19	-	-
Sr	118	-	0.000690	-	0.0831	-	0.0118	-	0.0703	-	0.012	-	0.00467	-	0.0453	-	-
B	27	-	0.00591	-	0.130	-	0.154	-	0.109	-	0.0426	-	0.082	-	0.0814	-	-
Al	53.5	0.631	0.631	0.165	0.176	0.0433	0.0749	0.124	0.182	0.0949	0.098	0.0295	0.0221	0.0761	0.0768	-	-
Sc	74.5	-	0.287	-	4.46	-	0.913	-	4.89	-	1.61	-	0.357	-	0.847	-	-
V	64.0	-	3.92	-	0.883	-	0.192	-	0.771	-	0.303	-	0.0886	-	0.224	-	-
Cr	61.5	-	27700	-	156	-	153	-	706	-	481	-	137	-	530	-	-
Ga	62.0	-	1.99	-	0.331	-	0.145	-	0.288	-	0.410	-	-	-	-	-	-
Y	90.0	-	-	-	0.758	-	0.120	-	0.653	-	0.0895	-	0.00752	-	0.106	-	-
<sup>28</sup> Si	16	-	-	-	2.55	-	-	-	4.10	-	4.04	-	0.421	-	-	-	-
<sup>29</sup> Si	40	-	0.0000993	0.861	0.861	0.880	0.880	0.868	0.868	0.878	0.878	0.888	0.888	0.879	0.879	-	-
<sup>30</sup> Si	40	-	0.0000813	0.861	0.856	0.880	0.880	0.868	0.847	0.878	0.841	0.888	0.864	0.879	0.867	-	-
Ti	60.5	-	0.000113	0.861	0.871	0.880	0.837	0.868	0.834	0.878	0.852	0.888	0.862	0.879	0.843	-	-
Zr	72	-	0.404	0.286	0.329	-	0.0985	0.429	0.329	-	0.133	-	0.0193	-	0.105	-	-
P	38	-	-	-	0.258	-	0.382	-	0.127	-	0.0309	-	-	-	0.0710	-	-
As	46	-	0.0509	-	0.0353	-	0.153	-	0.0539	-	0.0244	-	0.0255	-	0.0478	-	-
OH	137	-	0.116	-	0.334	-	0.444	-	0.347	-	0.323	-	0.598	-	0.189	-	-
F <sup>a</sup>	133	-	0.0297 <sup>f</sup>	-	0.404 <sup>f</sup>	-	0.297 <sup>f</sup>	-	0.233 <sup>f</sup>	-	0.205 <sup>f</sup>	-	0.176 <sup>f</sup>	-	0.244 <sup>f</sup>	-	-
OH <sup>a</sup>	137	-	0.217 <sup>f</sup>	-	1.53 <sup>f</sup>	-	8.34 <sup>f</sup>	-	1.37 <sup>f</sup>	-	1.66 <sup>f</sup>	-	1.01 <sup>f</sup>	-	1.24 <sup>f</sup>	-	-
F <sup>a</sup>	133	-	0.0297 <sup>f</sup>	-	0.404 <sup>f</sup>	-	0.297 <sup>f</sup>	-	0.233 <sup>f</sup>	-	0.205 <sup>f</sup>	-	0.176 <sup>f</sup>	-	0.244 <sup>f</sup>	-	-
Cl <sup>a</sup>	181	-	0.0553 <sup>f</sup>	-	0.315 <sup>f</sup>	-	0.0997 <sup>f</sup>	-	0.204 <sup>f</sup>	-	0.260 <sup>f</sup>	-	0.0711 <sup>f</sup>	-	0.103 <sup>f</sup>	-	-
O	140	0.908	-	0.960	-	0.961	-	0.961	-	0.962	-	0.961	-	0.961	-	-	-
S <sup>a</sup>	184	-	-	-	11	-	2.19 <sup>f</sup>	-	9.67 <sup>f</sup>	-	2.28 <sup>f</sup>	-	0.349 <sup>f</sup>	-	1.77 <sup>f</sup>	-	-
S <sup>a</sup>	184	-	0.298 <sup>f</sup>	-	0.574 <sup>f</sup>	-	2.16 <sup>f</sup>	-	0.617 <sup>f</sup>	-	1.60 <sup>f</sup>	-	0.347 <sup>f</sup>	-	0.611 <sup>f</sup>	-	-
N	146	-	0.615	-	0.827	-	0.596	-	-	-	0.0521	-	0.173	-	2.20	-	-

Values determined by using secondary positive-ion detection of SIMS. <sup>a</sup> Values determined by using secondary negative-ion detection of SIMS.

<sup>b</sup> A part of the Fe is in the trivalent state with ionic radius of 64.5 pm. <sup>c</sup> Shannon (1976). <sup>d</sup> Molar ratio.

<sup>e</sup> Relative ion intensity ratio normalized for <sup>28</sup>Si. <sup>f</sup> Relative ion intensity ratio normalized for <sup>19</sup>F of positive-ion detection.

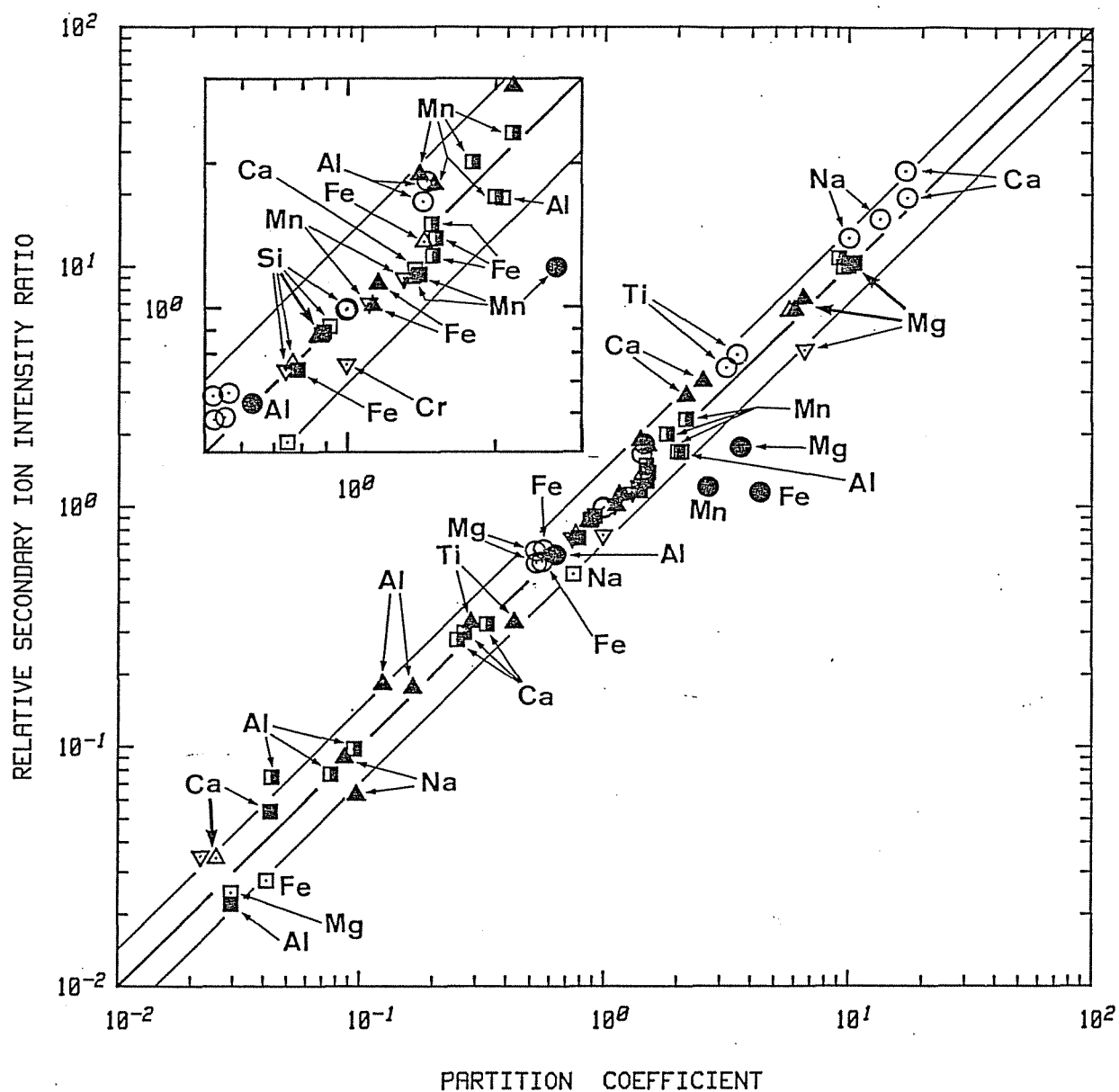


Fig. II-5 The relation between the relative secondary ion intensity and the partition coefficient measured by EPMA.

- △: Olivine/groundmass (Yurimoto and Sueno, 1984a)
- ▽: Olivine/groundmass (Yurimoto and Sueno, unpublished)
- : Plagioclase/groundmass (Yurimoto and Sueno, 1984a)
- : Bronzite/augite (Chapter III)
- : Protoenstatite/groundmass (This study)
- ▤: Bronzite/groundmass (This study)
- ▲: Augite/groundmass (This study)
- : Chrome spinel/groundmass (This study)

the detection limit of the EPMA analysis. As shown in Fig. II-5, all relative ion intensity ratios have the values corresponding to the partition coefficients measured by EPMA within a  $\pm 30\%$  error, except for spinel-glass system. The relative ion intensity ratios for trace elements are also consistent with partition coefficients reported previously (e.g., Henderson, 1982). The error value does also agree with the value of the matrix effect given in Ray and Hart (1982).

The larger matrix effect of the spinel-glass system may be due to the difference of Si concentration, that is, Si concentration of the spinel crystal is under detection limit of EPMA analysis, but the groundmass glass belong to silicate material. Nevertheless the relative ion intensity ratios of the spinel-glass system have the values within 0 to  $-60\%$  error except for Fe as shown in Fig. II-5. The range of error is relatively shifted  $-30\%$  from the other mineral systems, but the internal consistency holds as same as the other systems. Further the relative ion intensity ratios for trace elements are also consistent in order with partition coefficients reported previously (e.g., Irving, 1978). These evidences suggest that the correspondence between the relative ion intensity ratio and partition coefficient remains within  $\pm 30\%$  error as internal coherency of relative ion intensity ratio: although the error value is shifted by the element species of normalization. The only exception detected is Fe value in spinel-glass system. Because secondary ion yield of trivalent iron would have different value from divalent iron, the anomaly of Fe may be due to the existence of Fe as trivalent state in significant amount in the spinel crystal in addition to divalent state in the spinel crystal. Assuming

stoichiometry, it is expected that about 20% of total iron content is in trivalent state in spinel crystal (calculated from Table II-1).

Therefore, we can assume, as a first approximation, that the measured relative ion intensity ratios are equivalent to the partition coefficients within about 30% error in average: although the verification of this assumption needs further development of quantitative techniques for SIMS. The partition coefficients for the spinel-glass system may be estimated to be about 30% excessive in this study.

The results obtained in this study are shown in Figs. II-6, II-7, II-8 and II-9 as PC-IR diagrams for bronzite-, protoenstatite-, augite- and chrome spinel- groundmass systems, respectively. Because the ionic radius vs. coordination number plots are reasonably regular (Shannon, 1976), the regularity concluded for the six-fold coordinated radii remains unchanged for the radii of other coordination number. Ionic radius values for six-fold coordination by Shannon (1976) were used on the diagrams except for the value of N regardless of the actual coordination number around a crystallographic site in a given crystal. For the value of N, the ionic radius for four-fold coordination by Shannon (1976) was used because of absence of six-fold value.

## DISCUSSION

### Bronzite-groundmass system

PC-IR diagram for bronzite and bulk rock composition of boninite has been reported by Hirano et al. (1979). However, it is not clear whether their bronzite sample was in equilibrium with the boninite sample used because the bronzite sample was collected from bronzite

sands at Hatsune-ura, Chichi-jima, Bonine Islands, and the groundmass phase in the boninite sample was not separated.

New PC-IR diagrams for bronzite and groundmass in boninite are shown in Fig. II-6. The partitioning patterns and partition coefficients reported by Hirano et al. (1979) are in good agreement with those in this study. This agreement gives strong support that the equilibrium are nearly achieved between the bronzite and bulk rock composition of boninite reported by Hirano et al. (1979). As shown in Fig. II-6, most of partition coefficients for three kinds of bronzites have essentially the equivalent values. The agreement again showed that the bronzites and groundmass glass are in equilibrium one another.

The crystal structure of Ca-poor pyroxene is based on distorted cubic close-packed array of oxygen (Matsui, 1979) and can be basically described by four crystallographically-distinct sites, i.e., sites for four-coordinated cations (T sites), six-coordinated cations (M1 and M2 sites), and anions (X sites), which are mainly occupied in nature by  $\text{Si}^{4+}$ ,  $\text{Mg}^{2+}$  and  $\text{Fe}^{2+}$ , and  $\text{O}^{2-}$ , respectively. It is well established that  $\text{Mn}^{2+}$ ,  $\text{Fe}^{2+}$ ,  $\text{Mg}$ ,  $\text{Fe}^{3+}$ ,  $\text{Al}$ ,  $\text{Cr}$  and  $\text{Ti}$  in the M1 site;  $\text{Na}$ ,  $\text{Ca}$ ,  $\text{Mn}^{2+}$ ,  $\text{Fe}^{2+}$ ,  $\text{Mg}$  and  $\text{Li}$  in the M2 site; and  $\text{Si}$  and  $\text{Al}$  in the T sites in pyroxenes (Cameron and Papike, 1980). In bronzite structure,  $\text{Fe}^{2+}$  ions prefer the M2 site whereas  $\text{Mg}^{2+}$  ions the M1 site, and  $\text{Al}^{3+}$  ions prefer the TB site whereas  $\text{Si}^{4+}$  ions the TA site (Takeda, 1972).

Matsui et al. (1977) reported the PC-IR diagram (originally Onuma et al., 1968) for bronzite-groundmass system in an alkali-olivine basalt. They presented that partition patterns for divalent and trivalent cations could be seen as composed of two parabolas, one with its peak located near 70  $\mu\text{m}$  and another with the peak located near 85



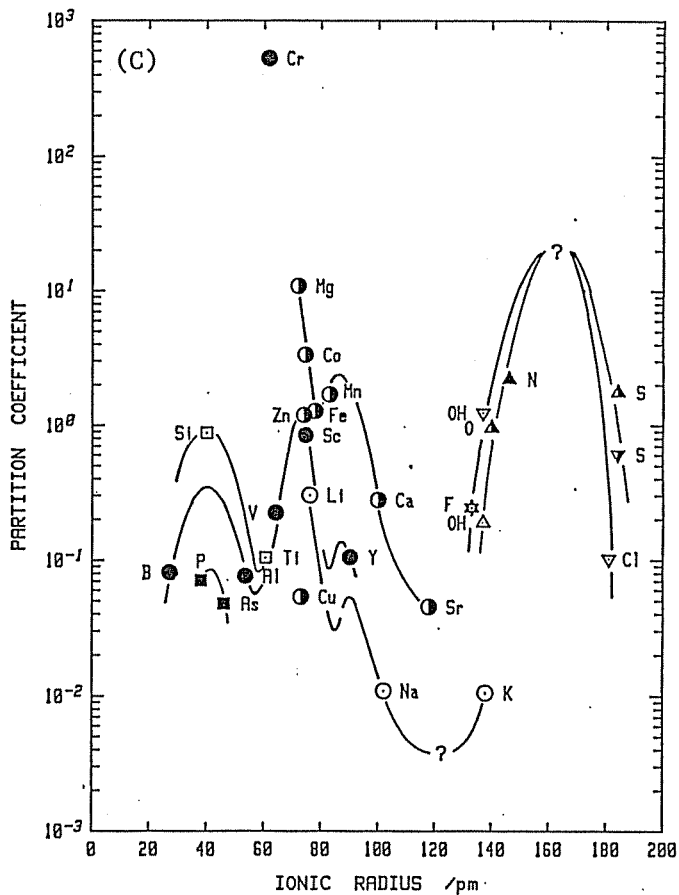
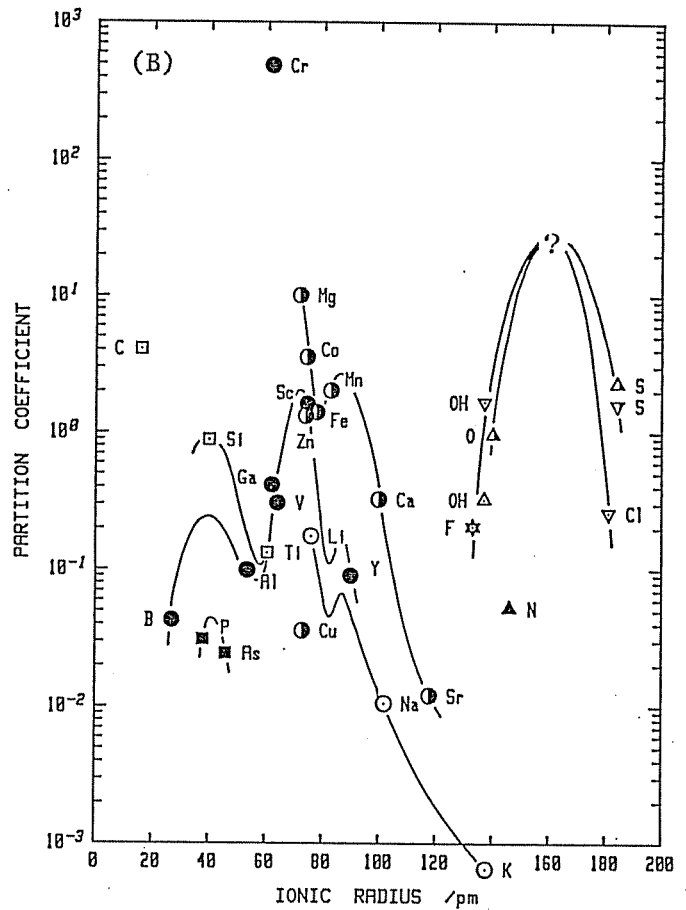
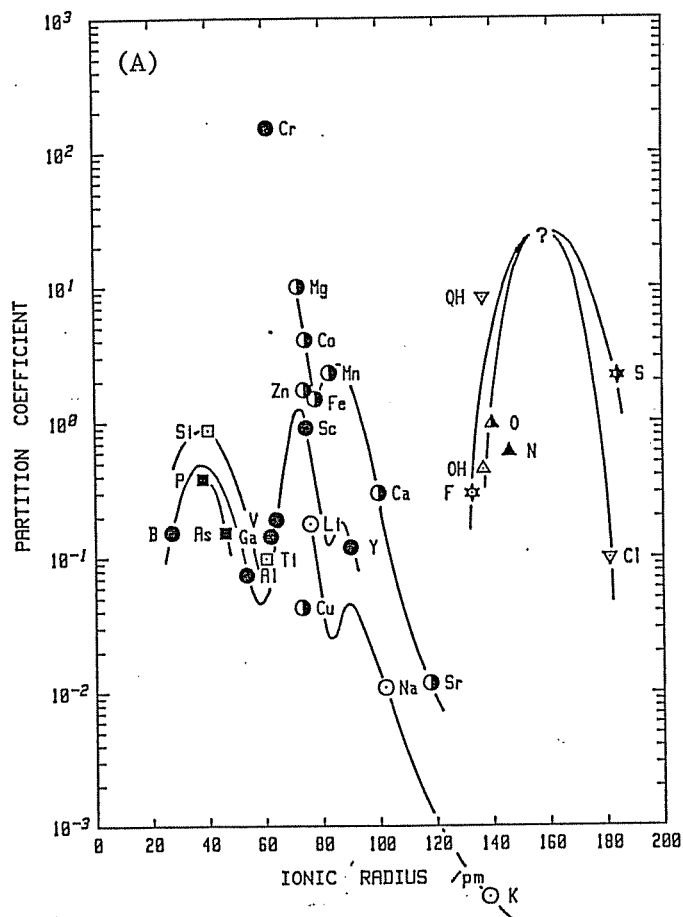


Fig. II-6 Partition coefficient-ionic radius diagram for bronzite-groundmass system. (A) CJ-02A, (B) CJ-02B and (C) CJ-02C.

Symbols are the same as in Fig. I-1.

pm. The former peak was assigned to the M1 site, and the latter to the M2 site although the M2 peak appeared only as a shoulder upon the conspicuous M1 peak. In Fig. II-6 the curve for divalent cations can be clearly observed as two parabola peaks, one with its peak corresponding to M1 site near 70 pm and another with the peak corresponding to M2 site near 85 pm. The M1 peak was also confirmed by the trivalent curve with the peak near 70 pm between  $\text{Sc}^{3+}$  and  $\text{V}^{3+}$ . The peak positions for the M1 and M2 sites are unchanged in spite of the difference of bulk chemistry and physical condition between the systems; the bronzite crystal used by Matsui et al. (1977) contains the unusually high alumina composition and it is estimated that the aluminous bronzite equilibrated with the alkali-olivine basalt magma under a pressure of about 10 kbar (Kuno, 1965), whereas it is estimated that the bronzite crystal in boninite equilibrated with the boninite magma under a pressure of below 5 kbar and a temperature about over 1000°C in hydrous condition (Kuroda et al., 1978). Owing to insufficient number of rare earth elements analyzed it is impossible to draw exactly the righthand half of the M1 peak and the M2 peak for trivalent ions. However, it is conceivable to suppose a minimum and a maximum on the trivalent curve between  $\text{Sc}^{3+}$  and  $\text{Y}^{3+}$  plots as shown in Fig. II-6 according to the curve for divalent cations in Fig. II-6 and the curve for trivalent cations reported Matsui et al. (1977). The partition coefficients for  $\text{Li}^+$ ,  $\text{Na}^+$  and  $\text{K}^+$  decrease in this order except for the epitaxial bronzite on protoenstatite (Fig. II-6C), but it is also conceivable to suppose a minimum and a maximum on the monovalent curve between  $\text{Li}^+$  and  $\text{Na}^+$  plots as shown in Fig. II-6, i.e., the curve from  $\text{Na}^+$  to  $\text{K}^+$  should be the righthand slope of M2 peak. In the epitaxial bronzite (Fig. II-6C) the partition coefficients for  $\text{Na}^+$

and  $K^+$  are roughly equal. The reason is discussed at the following section.

The bronzite structure has two kinds of T sites called TA and TB. TA and TB sites have very similar configuration around them and metal-oxygen distances, the mean TB-O distance being only about 1.2 pm and 1.8 pm larger than the mean TA-O distance in enstatite and bronzite, respectively (Table II-4). Because only eleven ions ( $Be^{2+}$ ,  $B^{3+}$ ,  $Al^{3+}$ ,  $C^{4+}$ ,  $Si^{4+}$ ,  $Ti^{4+}$ ,  $Ge^{4+}$ ,  $P^{5+}$ ,  $As^{5+}$ ,  $Mo^{6+}$  and  $W^{6+}$ ) have the ionic radii for six-fold coordination less than 60 pm in terrestrial materials, it is difficult to define the exact shape of the curve for homovalent ions less than 60 pm. Therefore the peak corresponding to the TA and TB sites should be overlapping completely with each other. In Fig. II-6 the curves for trivalent, tetravalent and pentavalent cation strongly suggest the existence of the TA plus TB peak located near  $Si^{4+}$  plot. The partition coefficients for pentavalent cations and  $Cr^{3+}$  of the bronzite phenocryst partially overgrown by augite (Fig. II-6A) have higher and lower values than that of other bronzite crystals (Fig. II-6A and B), respectively. The anomalies may be due to compositional heterogeneities or kinetic effects of crystal growth for the ions because the similar anomalies are also observed for the overgrown augite on the bronzite crystal (Fig. II-7A). Nevertheless the partition pattern for pentavalent cations is consistent with the curve for other valence cations.

The peaks of the X sites are displayed for monovalent and divalent anions in Fig. II-6 and are drawn so as to make the parabola-shaped lines as smooth as possible. The position of the X peak seems to be larger than the ionic radius of  $O^{2-}$ , but owing to the absence of the

Table II-4 Comparison of the mean interatomic distances (pm) in pyroxene and spinel

	P-En	C-En	O-En	Br	Di		Aug	Sp
	1080°C	R.T.	R.T.	R.T.	R.T.	1000°C	R.T.	R.T.
<M(1)-O>	212.1	207.8	207.8	207.0	207.7	210.7	205.7	192.7**
<M(2)-O>	219.1	214.2	215.1	217.6	242.5 <sup>#</sup>	245.2 <sup>#</sup>	239.9 <sup>#</sup>	
					(249.8)	(253.8)	(248.2)	
<Si-O>	162.6	163.4	163.4	163.6	163.4	163.7	164.4	191.9***
<SiA-O>		162.8	162.8	162.7				
<SiB-O>		163.8	164.0	164.5				

P-En: proto-enstatite (Murakami *et al.*, 1982), C-En: clino-enstatite (Ohashi and Finger, 1976),

O-En: ortho-enstatite (Sasaki *et al.*, 1982), Br: Aluminan Bronzite (Takeda, 1972),

Di: diopside (Di at R.T.: Clark *et al.*, 1969; Di at 1000°C: Cameron *et al.*, 1973),

Aug: Augite (Takeda, 1972), Sp: Spinel (Yamanaka and Takeuchi, 1983).

R.T.: room temperature. <sup>#</sup> Six-coordinated value.

( ): Eight-coordinated value. \*\*<B-O>. \*\*\*<A-O>.

monovalent and divalent anions with radii between those of  $O^{2-}$  and  $Cl^{-}$  it is impossible to define exactly the position of the peak.

Among the divalent cations analyzed, the significant deviation from the smooth curve is observed in  $Zn^{2+}$  and  $Cu^{2+}$ . The deviation are ascribed to the well-known tetrahedral (Matsui et al., 1977) and square planner coordination (Yurimoto and Sueno, 1984a) preferences of  $Zn^{2+}$  and  $Cu^{2+}$ , respectively. Among trivalent cations,  $Cr^{3+}$  shows a marked deviation from regularity, and this is ascribed to the strong crystal field effect in  $Cr^{3+}$  ions (Matsui et al., 1977). Among tetravalent cations,  $C^{4+}$  shows a deviation from the smooth curve, and this may be ascribed that  $C^{4+}$  ions occupy the interstitial site or exist as inclusions of sub-microscopic size in the bronzite crystal.

#### Protoenstatite-groundmass system

In the protoenstatite all the tetrahedral site are equivalent (T site and are very similar to TA site of orthoenstatite in configuration around them and in available space. The protoenstatite M2 site is less flexible than orthopyroxene M2 site because the orthopyroxene M2 site has a considerably displaced bridging oxygen (O3B) in addition to a less displaced one (O3A) whereas all bridging oxygens coordinated to the protoenstatite M2 site are the less displaced ones (O3) and M2 can not be expand anymore (Murakami et al., 1982). Therefore in the protoenstatite-groundmass system we can expect well defined M1 peak and less prominent M2 peak than the bronzite M2 peak. Further because  $Al^{3+}$  ions do not prefer the TA site of bronzite (Takeda, 1972), the partition coefficient of  $Al^{3+}$  should have smaller value than that of bronzite.

Fig. II-7 is the PC-IR diagram for protoenstatite-groundmass system. As expected, partition pattern for divalent cations have

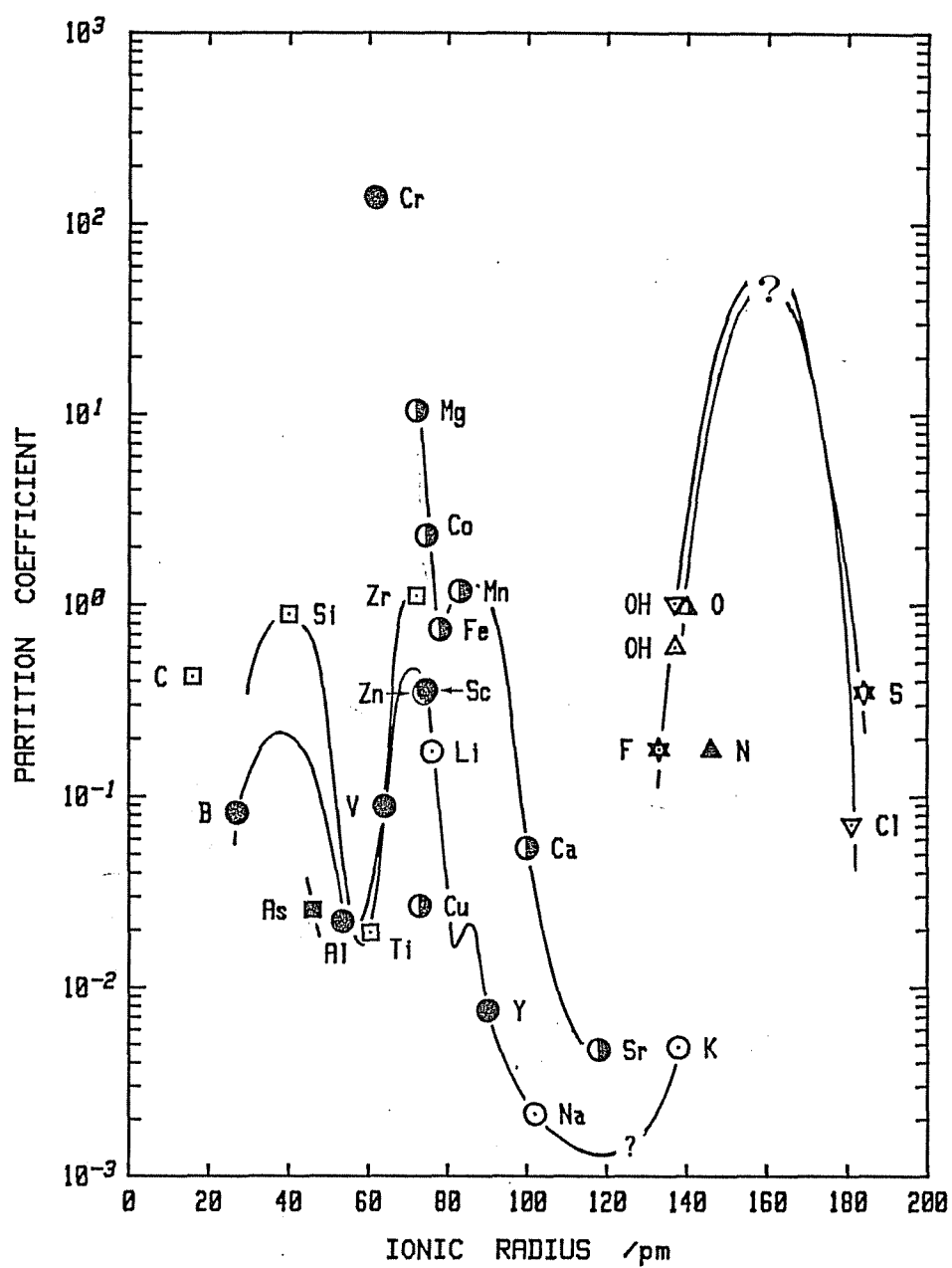


Fig. II-7 Partition coefficient-ionic radius diagram for protoenstatite-groundmass system. Symbols are the same as in Fig. I-1.

conspicuous and small peaks, which correspond to the M1 and M2 sites, respectively. The M1 peak is also constructed by the curve for trivalent cation. The curve from  $\text{Ti}^{4+}$  to  $\text{Zr}^{4+}$  shows the left-hand half slope of the M1 peak. The curves for monovalent and trivalent cations can be drawn a minimum and a maximum between  $\text{Li}^+$  and  $\text{Na}^+$  and between  $\text{Sc}^{3+}$  and  $\text{Y}^{3+}$ , as shown in Fig. II-7, according to the discussion of the bronzite-groundmass system. The peak positions of M1 and M2 sites have the radii with about 70 pm and 85 pm, respectively.

The partition coefficient for  $\text{K}^+$  have slightly higher value than that for  $\text{Na}^+$  (Fig. II-7). The similar tendency for  $\text{K}^+$  are observed in the epitaxial bronzite on the protoenstatite-groundmass system (Fig. II-6C). The partition coefficients for  $\text{K}^+$  in both systems are roughly equal whereas the partition coefficient for  $\text{Na}^+$  in the protoenstatite - groundmass system is considerably lower than that in the epitaxial bronzite-groundmass system. The anomal distribution for  $\text{K}^+$  may be due to the influence of submicroscopic inclusions with high K content. The idea is also suggested by the following evidences: the inverted protoenstatite crystal has conspicuous cracks formed during the proto to clino transformation. The epitaxial bronzite has also considerable cracks which may be formed by a strain with the proto to clino transformation of the base crystal. Yasuda et al. (1983) reported that the cracks in inverted protoenstatite in boninite were filled with fibrous crystals.

The T peak appears around  $\text{Si}^{4+}$  according to the superposition of the curves for trivalent and tetravalent cations. The partition coefficient for  $\text{As}^{5+}$  seems to be located on the right-hand slope of the T peak. As expected, the partition coefficient for  $\text{Al}^{3+}$  has smaller

value than that of bronzite, but the partition coefficient for  $B^{3+}$  is less affected by the structural differences between proto and ortho pyroxenes. If this interpretation and the symmetrical shape for the T peak are accepted, the peak position of T site may be slightly sifted from  $Si^{4+}$  to the smaller direction of the ionic radius.

The curves for monovalent and divalent anions can be seen as one parabola-shaped peak. The position of the X peak seems to be larger than the ionic radius of  $O^{2-}$ . The partition coefficients for  $Cl^{-}$  and  $S^{2-}$  have smaller values than those of bronzite-groundmass system. It is conceivable that the protoenstatite X site has less tolerance to accommodate large anions.

#### Augite-groundmass system

The C2/c clinopyroxene structure can be basically described by the T, M1, M2 and X sites such as protoenstatite structure. However the C2/c clinopyroxene structure can be no longer constructed by close packing of oxygen because of M2 site occupied by  $Ca^{2+}$  ions. In nature the T, M1, M2 and X sites are mainly occupied by  $Si^{4+}$ ,  $Mg^{2+}$  and  $Fe^{2+}$ ,  $Ca^{2+}$ , and  $O^{2-}$ , respectively. The geometrical contrast between the M1 and M2 sites is much more enhanced in the C2/c clinopyroxene structure than in the Ca-poor pyroxene structure (Matsui et al., 1977). On the other hand, all the tetrahedral sites are equivalent (T site) and are very similar to TB site of orthoenstatite in anion configuration and T-O distances.

Matsui et al. (1977) reported the PC-IR diagram (originally by Onuma et al., 1968) for augite-groundmass system in an alkali-olivine basalt. They presented the conspicuous M1 and M2 peaks for monovalent, divalent and trivalent cations, the M1 peak located near 70  $\mu m$  and the



M2 peak located near 95  $\mu\text{m}$ . Fig. II-8 is the PC-IR diagram for augite-groundmass system in boninite. Partition pattern between Figs. II-8A and B have essentially the equivalent shape. As described by Matsui et al. (1977) the M1 and M2 peak is confirmed by the curves for monovalent, divalent and trivalent cations. The peak position for M1 and M2 sites are unchanged in spite of the difference of bulk chemistry and physical conditions of each system; the difference is already described in the section of bronzite-groundmass system. The T peak is observed around  $\text{Si}^{4+}$  according to the superposition of the curves for trivalent, tetravalent and pentavalent cations. It is conceivable that the augite T site is slightly flexible to accommodate larger cation as compared with the tetrahedral sites of bronzite and protoenstatite, because the partition coefficient for  $\text{Al}^{3+}$  and  $\text{Ti}^{4+}$  have higher values than that of bronzite.

The curves for homovalent anions compose the X peak which position is larger than the ionic radius of  $\text{O}^{2-}$ . The partition coefficient for  $\text{S}^{2-}$  has the largest values in the three pyroxenes analyzed. It may be suggested that the augite X site has one of the most tolerance to accommodate large anions in the pyroxene polymorphs.

The deviation from the smooth curve is observed in  $\text{Zn}^{2+}$ ,  $\text{Cu}^{2+}$ ,  $\text{Cr}^{3+}$  and  $\text{C}^{4+}$ . The reason for the deviations are ascribed to the characteristics of the ions as noticed already.

#### Chrome spinel-groundmass system

The spinel structure is based on distorted cubic close-packed array of anions (X site) in which one-eighth of the tetrahedral (A site) and one-half of the octahedral (B site) interstices are occupied by cation (Bragg, 1915; Nishikawa, 1915). The A and B sites have very similar

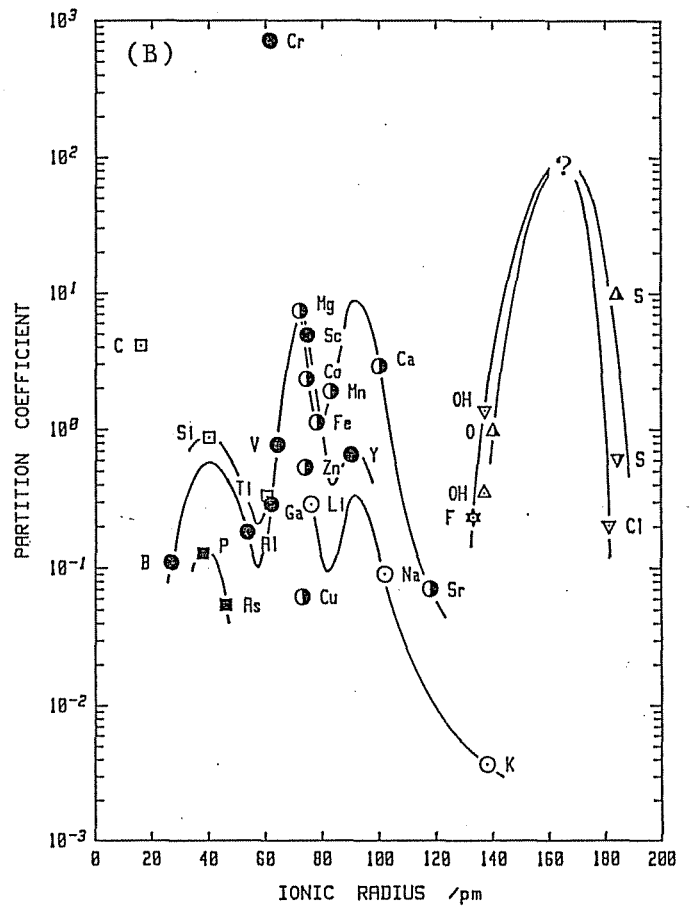
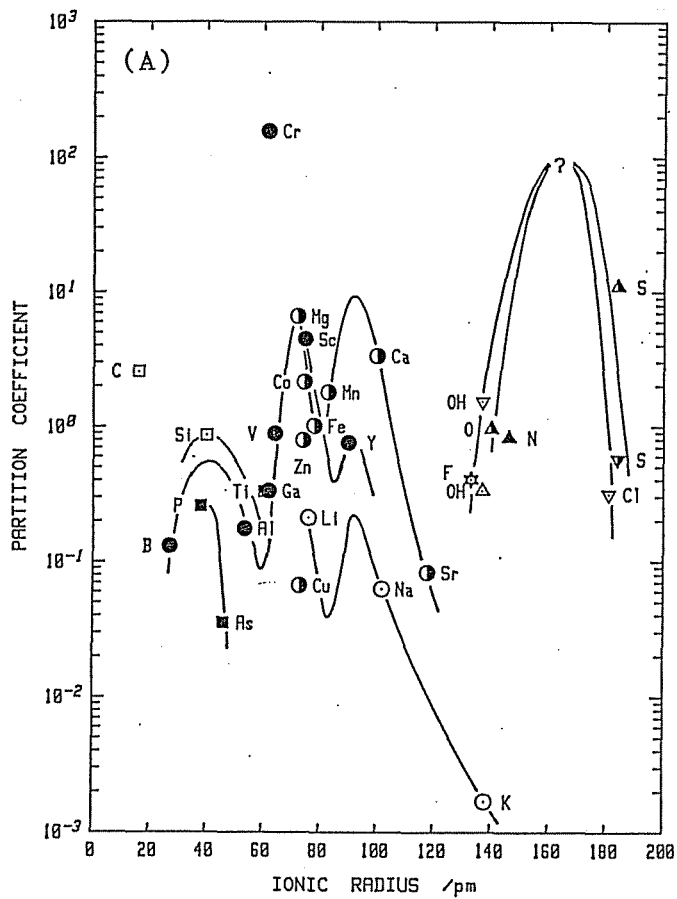


Fig. II-8 Partition coefficient-ionic radius diagram for augite-groundmass system. (A) CJ-02A and (B) CJ-02B. Symbols are the same as in Fig. I-1.

metal-oxygen distances, the B-O distance being only about 0.4 pm longer than the A-O distance in pure spinel crystal (Yamanaka and Takeuchi, 1982). However, the larger  $Mg^{2+}$  ion occupies A site whereas the smaller  $Al^{3+}$  ion occupies B sites (Bacon, 1952; Fischer, 1967). Therefore, in the spinel-groundmass system we can expect the appearance of three peaks corresponding to the A, B and X sites.

The PC-IR diagram for chrome spinel-groundmass system of boninite is shown in Fig. II-9. The preliminary results of this system have been reported by Yurimoto and Sueno (1984b). As expected, partition patterns for divalent and trivalent cations have separately constructed two peaks in PC-IR diagram, which almost certainly correspond to the A and B sites, respectively. The curve for monovalent cations shows the right-hand half slope of the A peak. The curve for tetravalent cations indicates the left-hand half of the B peak. The optimum sizes for the A and B sites have the six- (four-) coordinated radii of about 75 pm (60 pm: inferred from the four coordinated values of  $Co^{2+}$  and  $Li^{+}$ ) and 65 pm, respectively. The very steep slopes of both peaks strongly suggested that the spinel structure is intolerant of larger and smaller cations.

The partition coefficients for  $Na^{+}$  and  $K^{+}$  are roughly equal and the partition coefficient for  $Sr^{2+}$  are larger than for  $Ca^{2+}$ . The distribution for  $K^{+}$  and  $Sr^{2+}$  ions may be ascribed that those ions mainly occupy imperfections in spinel structure such as point defects and dislocation, and/or due to inclusions with submicroscopic size, as exemplified by the non-existence of the spinel structure including  $K^{+}$  and  $Sr^{2+}$  ions.

Similar to the previously described other phenocryst-groundmass systems, the deviation from the smooth curve is also observed for  $Cu^{2+}$ ,

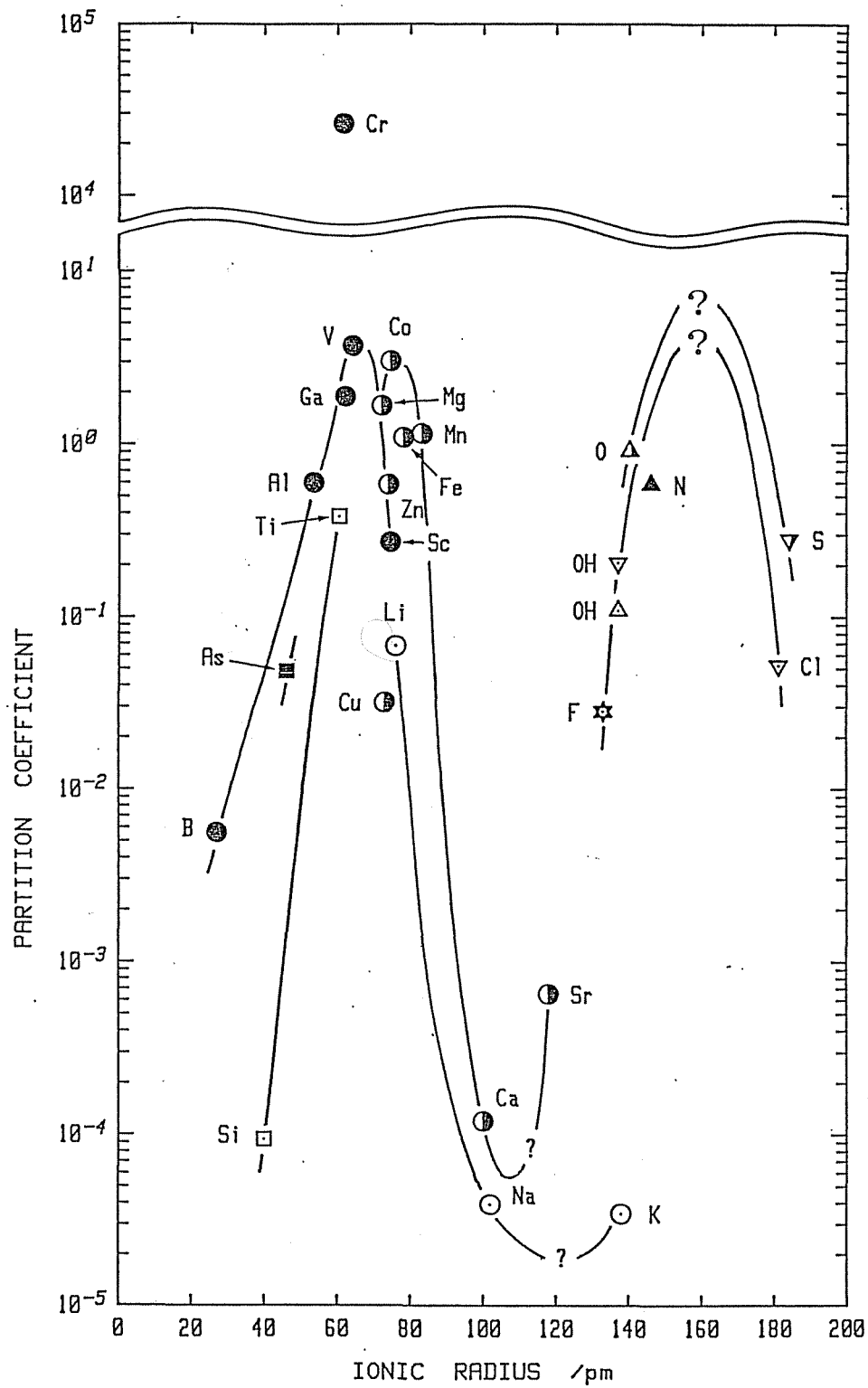


Fig. II-9 Partition coefficient-ionic radius diagram for spinel-groundmass system. Symbols are the same as in Fig. I-1.

$\text{Zn}^{2+}$  and  $\text{Cr}^{3+}$  in this spinel-groundmass system. The deviation for  $\text{Cu}^{2+}$  may be due to the square planar coordination preference of Cu ions (Yurimoto and Sueno; 1984a), but the deviation for  $\text{Zn}^{2+}$  is not understood by the tetrahedral preference of Zn ions (Matsui et al. 1977) because the ionic radius of  $\text{Zn}^{2+}$  is fitted in the A peak. Whereas  $\text{Cr}^{3+}$  ions are major components of this spinel crystal, very large discrepancy from the regular curve is observed. This evidence suggests that the crystal field stabilization energies play an important role in the solid/liquid partitioning for the spinel crystal. The deviation for Fe from the smooth curve is due to the uncertainty of SIMS analysis in this system noticed already.

As expected, partition pattern for monovalent and divalent anions have one peak, which is correspond to the X site. Similar to the other phenocryst-groundmass systems, the peak position for X site does not coincide with the plot of  $\text{O}^{2-}$ .

#### Comparison of partition coefficients among pyroxenes

The proto-, ortho- and C2/c clino- pyroxenes have four peaks on PC-IR diagrams corresponding to the T, M1, M2 and X site of the pyroxene structure (Fig. II-6, II-7, II-8 and II-9).

The position (about 70 pm) for the M1 peak is unchanged among the pyroxene polymorphs analyzed in spite of the difference of the chemical composition and physical condition of the system. The width of the M1 peak, which may correspond to the tolerance of the site, are unchanged among the polymorphs although the trivalent peak shift vertically. These interpretations are in harmony with the results of crystal structure analyses, i.e., the mean M1-O distances have the almost fixed

value at a given temperature (table 4). However, the values of M2 peak for the proto-, ortho- and C2/c clino- pyroxenes increase from 85 to 95 pm in this order. Because the proto- and ortho- pyroxene structures are based on nearly cubic close-packed array of oxygen, the M2 values for these two pyroxenes have nearly same value. On the other hand the M2 peak position for C2/c clinopyroxene have a large shift which may be due to the eight-fold coordination of anion for the M2 site. The order of the M2 shift is consistent with the mean M2-O distances as shown in Table II-4. The tolerances of the M2 sites among the pyroxene polymorphs inferred from the crystal structures are confirmed by the partition coefficients of the right-hand slope of the M2 peak, especially the M2 site for protoenstatite is intolerant of larger cations as nearly same as the case of olivine (Yurimoto and Sueno, 1984a).

The position of the T peak is nearly unchanged around  $\text{Si}^{4+}$  plots. However, the tolerance of T site increase in the order of the proto-, ortho- and C2/c clino- pyroxene, because the partition coefficients for  $\text{Al}^{3+}$  and  $\text{Ti}^{4+}$  increase in that order inspite of the fixed value of the partition coefficient for  $\text{Si}^{4+}$ . There are two kinds of the tetrahedrons in actual pyroxene structure, small one corresponding to the orthopyroxene TA site and the protopyroxene T site, and another corresponding to the orthopyroxene TB site and the C2/c clinopyroxene T site. The small tetrahedron naturally exhibits a strong site preference of  $\text{Si}^{4+}$  over  $\text{Al}^{3+}$  (Takeda, 1972). This evidence from the X-ray structure determination is consistent with the order of tolerance of T site.

Because the substitution of  $\text{Al}^{3+}$  for  $\text{Si}^{4+}$  in the pyroxene T site violates the Pauling's electrostatic valence rule (Pauling, 1929), in

order to maintain charge balancing, the M1 and M2 curves for trivalent cations move upward in the order of proto-, ortho- and clino- pyroxene. If this interpretation of the charge balancing ascribed to the substitution of  $\text{Al}^{3+}$  in the T sites and the strong M1 site preference of  $\text{Cr}^{3+}$  ions by crystal field effect (Burns, 1970) are accepted, the order in the strong enrichment of  $\text{Cr}^{3+}$  ion in pyroxene polymorphs can be also interpreted. Further the little enrichments of  $\text{Cr}^{3+}$  and  $\text{Sc}^{3+}$  in olivine crystal (Yurimoto and Sueno, 1984a) can be also interpreted, because the olivine crystal generally does not contain  $\text{Al}^{3+}$  ion (Brown, 1982).

The peak positions of the X site seems to be larger than the ionic radius of  $\text{O}^{2-}$  in the pyroxene polymorphs, but owing to the absence of the anions with radii between those of  $\text{O}^{2-}$  and  $\text{Cl}^-$ , it is impossible to define the exact position of the peak. The feature of the peak position is also confirmed to other silicate and oxide mineral-magma systems reported Yurimoto and Sueno (1984a) and in this study.

The peak position for the cation curve is assumed to present an optimum ion size for the crystallographic site in the mineral (Onuma et al., 1968). This assumption is useful for discussion of the partitioning of cation, and have been confirmed empirically. It seems that the empirical basis of this assumption is Pauling's first rule (Pauling, 1929): A coordination polyhedron of anions is formed about each cation, the cation-anion distance equaling the sum of their characteristic packing radii and their radius ratio determining both the nature of the coordination polyhedron and therefore the coordination number of the cation. However, it is considerable that each anion is mainly surrounded by anion, because the volume of anion is dominant in crystal structures and the volume of most cations is negligible except for the alkali and alkaline earth ions. Because the anion and anion

distance is highly variable even in a given mineral( e.g., from 255.3 to 338.5 pm in forsterite, Takeuchi et al., 1982) Pauling's first rule can not apply to the anion coordination polyhedron around anion. The anion porosities (Dowty, 1980) of oxides and silicates are also highly variable and always greater than the anion porosity of ideally close-packed spheres, assuming standard radii for oxygen, as the anions repel each other . Further the six-coordinated ionic radii for  $\text{Cl}^-$  and  $\text{S}^{2-}$  (Shannon, 1976) may be inconsistent with other values in Shannon's table because he picked up the values for  $\text{Cl}^-$  and  $\text{S}^{2-}$  from Pauling's (1960) crystal radius.

These evidences suppose that it is difficult to evaluate whether the peak position for X site represent an optimum anion size in crystal or not. Nevertheless the partition coefficient of  $\text{S}^{2-}$  for proto- ortho- and C2/c clino- pyroxene clearly increase in this order. This order is consistent with the order of increase in the possible displacement of the bridging oxygen O(3) and with that of the distortion from the close packing of oxygen. It suggest that the X site in pyroxene structure become more tolerance in order of proto-, orth- and C2/c clino pyroxene. For the empirical evidence in pyroxene the assumption for the peak position may be applicable to anion sites.



#### IV. EXSOLUTION/MATRIX PARTITIONING IN PYROXENE CRYSTALS OF ULTRAMAFIC NODULE

##### Experimental

##### Sample

A nodule of websterite (TKW-03) was collected from alkali-olivine basalt in Takashima, North Kyushu, Japan. The websterite mainly consists of augite and bronzite, and was classified into Group II rock type described by Kobayashi and Arai (1981). In the bronzite grain (TKW-03-A), there are many blebby exsolved augite and augite exsolved lamellae, and, in augite grain (TKW-03-B), there are many blebby exsolved bronzite and bronzite lamellae (Fig. III-1). Augite/bronzite partition coefficients between the blebby and surrounding phases were measured on both side of the contact using SIMS and an electron micro-probe analyzer (EPMA).

##### SIMS analysis

The SIMS instrument used in this study is the Cameca IMS-3f ion-mass microanalyzer at the Chemical Analysis Center of the University of Tsukuba. A beam of  $O^-$  ions with net energy of 13.8 keV (for secondary positive-ion detection) and 8.1 keV (for secondary negative-ion detection) was focused with a spot 15-20  $\mu m$  in diameter on the gold-coated surface of a polished thin section. The vacuum of sample chamber is 0.5  $\mu Pa$ . The secondary ion intensities were measured by an electron multiplier coupled with pulse-counting circuitry with a

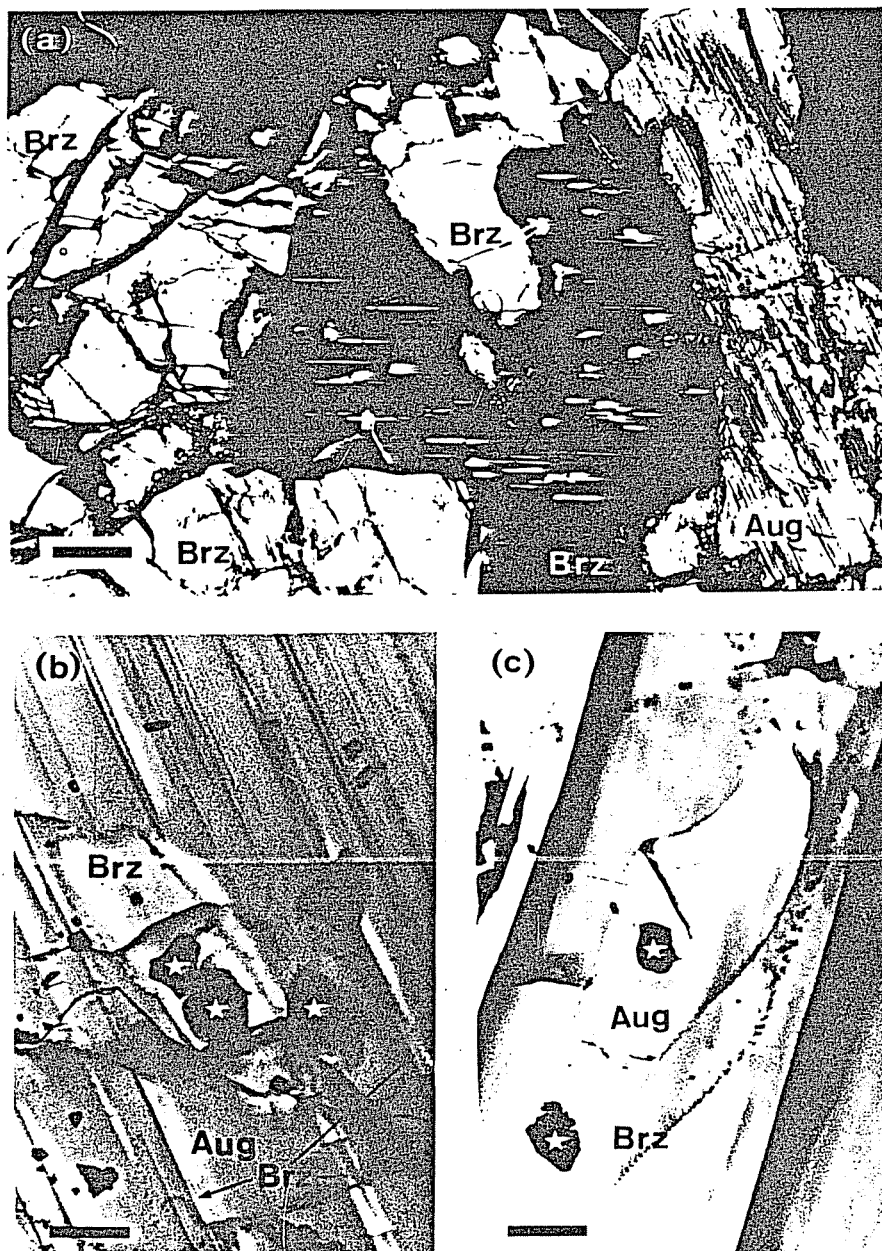


Fig. III-1 (a) Transmitted light photomicrograph of exsolved pyroxenes from specimen TKW-03. The length of the scale bar is 0.3 mm. Under polarized light. Aug=augite. Brz=bronzite.

(b) Transmitted light photomicrograph of specimen TKW-03-A. The length of the scale bar is 20  $\mu$ m. Under polarized light. ☆=trace of primary beam of SIMS analysis.

(c) Transmitted light photomicrograph of specimen TKW-03-B. The length of the scale bar is 20  $\mu$ m. Under polarized light.

mass resolution of about 5000, with the use of a cold trap of liquid nitrogen for more clean vacuum around the sample surface. Positive secondary ion intensity ratios relative to  $^{28}\text{Si}$  were measured for Li, Na, K, Mg, Ca, Mn, Fe, Co, Sr, Al, Sc, V, Cr, Y, C, Si, Ti, P, As, H, F, S and N. Negative secondary ion intensity ratios relative to  $^{28}\text{Si}$  were measured for H, F, Cl and S. Other experimental procedures were similar to those employed by Yurimoto and Sueno (1984a).

#### EPMA analysis

The EPMA system at the Chemical Analysis Center of the University of Tsukuba, which consists of a JXA50A (JEOL) main part and an ACPS-XR (ELIONIX) controlling part, was used with an accelerating voltage of 15 kV and a probe current of 0.014  $\mu\text{A}$  on a Faraday cage. A beam spot of about 1-2  $\mu\text{m}$  in diameter was used. The Bence and Albee (1968) method was applied to make quantitative analysis corrections. Other experimental conditions were similar to those employed by Yurimoto and Sueno (1984a).

#### Results

EPMA line analyses across the contact between blebby exsolved augite and bronzite matrix, and between the blebby bronzite and augite matrix showed no detectable compositional gradients for major elements on either side of the contact of both systems. The chemical compositions of each phase have essentially the equivalent values as shown in Table III-1. These evidences show that the equilibrium is achieved between the blebby exsolved and surrounding matrix phases in

Table III-1 Electron microprobe analyses of exsolution  
and the matrix pyroxenes

	TKW-03-A		TKW-03-B	
	Augite <sup>b</sup>	Bronzite <sup>c</sup>	Augite <sup>c</sup>	Bronzite <sup>b</sup>
SiO <sub>2</sub>	50.9 $\pm$ 0.5 <sup>d</sup>	53.2 $\pm$ 0.2	50.6 $\pm$ 0.2	53.3 $\pm$ 0.4
TiO <sub>2</sub>	0.73 $\pm$ 0.08	0.24 $\pm$ 0.04	0.94 $\pm$ 0.04	0.28 $\pm$ 0.23
Al <sub>2</sub> O <sub>3</sub>	7.40 $\pm$ 0.15	5.43 $\pm$ 0.12	7.09 $\pm$ 0.10	5.07 $\pm$ 0.18
FeO <sup>a</sup>	5.77 $\pm$ 0.12	10.6 $\pm$ 0.4	5.72 $\pm$ 0.15	10.7 $\pm$ 0.2
MgO	14.8 $\pm$ 0.3	29.4 $\pm$ 0.1	15.1 $\pm$ 0.2	29.8 $\pm$ 0.2
CaO	18.5 $\pm$ 0.2	1.11 $\pm$ 0.04	18.9 $\pm$ 0.2	1.15 $\pm$ 0.05
Na <sub>2</sub> O	1.45 $\pm$ 0.04	0.15 $\pm$ 0.03	1.55 $\pm$ 0.03	0.12 $\pm$ 0.03
Total	99.6	100.1	99.9	100.4
Oxygen = 6				
Si	1.86	1.87	1.85	1.87
Ti	0.0201	0.0064	0.0258	0.0074
Al	0.319	0.225	0.305	0.210
Fe	0.176	0.312	0.175	0.315
Mg	0.807	1.54	0.823	1.56
Ca	0.725	0.0419	0.740	0.0433
Na	0.103	0.010	0.110	0.0082
Total	4.01	4.01	4.03	4.01
<sup>a</sup> total iron as FeO. <sup>b</sup> matrix phase. <sup>c</sup> exsolution phase. <sup>d</sup> Standard deviation. Cr <sub>2</sub> O <sub>3</sub> , NiO, MnO and K <sub>2</sub> O: not detected.				

both augite-bronzite systems. These equilibrium parts were also analyzed by SIMS. Relative secondary ion intensities for the both systems are listed in Table III-2.

Partition coefficient values calculated from the values in Tables III-1 and III-2 are listed in Table III-3. The partition coefficient  $D(i)$  of a particular element  $i$  is defined as the ratio:  
$$D(i) = \frac{C_i^{\text{Cpx}}}{C_i^{\text{Opx}}}$$
where  $C_i^{\text{Cpx}}$  is the concentration of the element  $i$  in the augite phase at a particular stage,  $C_i^{\text{Opx}}$  is the concentration of the element  $i$  in the bronzite phase that is in equilibrium with the augite.

Ray and Hart (1982) recognized about 30% (in average) different yield of secondary ion for both major and trace elements between silicate glass and Ca-rich clinopyroxene. Such a matrix effect is probably recognized between the augite and bronzite in this study. However, Yurimoto and Sueno (1984a) found that the relative ion intensity ratios normalized for the  $^{28}\text{Si}$  value for olivine- and plagioclase- groundmass glass systems had the values corresponding to the partition coefficients. Relative ion intensity ratios between silicate phenocrysts and the groundmass glasses as well as between augites and bronzites in this study are plotted in Fig. III-2 against partition coefficients calculated by EPMA analyses. As shown in Fig. III-2, all relative ion intensity ratios have the values corresponding to the partition coefficients measured by EPMA within a  $\pm 30\%$  error, especially the relative ion intensity ratios for augite-bronzite systems have the values within 0 to  $+30\%$  error. The error value does also agree with the value of the matrix effect given in Ray and Hart (1982).

Table III-3. Partition coefficients of the elements between exsolution and the host pyroxenes

Element	Ionic radius <sup>c</sup> /pm	Partition coefficient			
		TKW-03-A		TKW-03-B	
		EPMA <sup>d</sup>	SIMS <sup>e</sup>	EPMA <sup>d</sup>	SIMS <sup>e</sup>
Li	76	-	1.63	-	2.85
Na	102	$1.00 \times 10^1$	$1.32 \times 10^1$	$1.34 \times 10^1$	$1.58 \times 10^1$
K	138	-	3.16	-	$1.38 \times 10^1$
Mg	72.0	$5.23 \times 10^{-1}$	$6.57 \times 10^{-1}$	$5.26 \times 10^{-1}$	$5.83 \times 10^{-1}$
Ca	100	$1.73 \times 10^1$	$1.94 \times 10^1$	$1.71 \times 10^1$	$2.51 \times 10^1$
Mn	83	-	$8.56 \times 10^{-1}$	-	$7.69 \times 10^{-1}$
Fe <sup>b</sup>	78	$5.65 \times 10^{-1}$	$6.63 \times 10^{-1}$	$5.55 \times 10^{-1}$	$5.90 \times 10^{-1}$
Co	74.5	-	$4.98 \times 10^{-1}$	-	$4.14 \times 10^{-1}$
Sr	118	-	$8.61 \times 10^1$	-	$1.47 \times 10^2$
Al	53.5	1.42	1.66	1.45	1.83
Sc	74.5	-	3.41	-	3.68
V	64.0	-	2.47	-	3.10
Cr	61.5	-	1.87	-	2.12
Y	90.0	-	$1.34 \times 10^1$	-	$1.08 \times 10^1$
C	16	-	$1.37 \times 10^{-1}$	-	-
<sup>28</sup> Si	40	$9.94 \times 10^{-1}$	$9.94 \times 10^{-1}$	$9.86 \times 10^{-1}$	$9.86 \times 10^{-1}$
<sup>29</sup> Si	40	$9.94 \times 10^{-1}$	$9.88 \times 10^{-1}$	$9.86 \times 10^{-1}$	$9.50 \times 10^{-1}$
<sup>30</sup> Si	40	$9.94 \times 10^{-1}$	$9.63 \times 10^{-1}$	$9.86 \times 10^{-1}$	$9.41 \times 10^{-1}$
Ti	60.5	3.16	3.80	3.49	4.31
P	38	-	1.43	-	3.21
As	46	-	2.16	-	5.63

Table III-3. (continued)

Element	Ionic radius <sup>c</sup> /pm	Partition coefficient			
		TKW-03-A		TKW-03-B	
		EPMA <sup>d</sup>	SIMS <sup>e</sup>	EPMA <sup>d</sup>	SIMS <sup>e</sup>
OH	137	-	3.05	-	-
F	133	-	2.29	-	-
OH <sup>a</sup>	137	-	2.95 <sup>f</sup>	-	9.15 x 10 <sup>-1f</sup>
F <sup>a</sup>	133	-	2.29 <sup>f</sup>	-	2.55 <sup>f</sup>
Cl <sup>a</sup>	181	-	2.25 <sup>f</sup>	-	1.42 <sup>f</sup>
O	140	1.00	-	9.99 x 10 <sup>-1</sup>	-
S	184	-	1.05 x 10 <sup>1</sup>	-	6.00
S <sup>a</sup>	184	-	4.06 <sup>f</sup>	-	3.64 <sup>f</sup>
N	146	-	-	-	1.46

Values determined by using secondary positive-ion detection of SIMS.

<sup>a</sup> Values determined by using secondary negative-ion detection of SIMS.

<sup>b</sup> A part of the Fe is in the trivalent state with ionic radius of 64.5 pm.

<sup>c</sup> Shannon (1976).

<sup>d</sup> Molar ratio.

<sup>e</sup> Relative ion intensity ratio normalized for <sup>28</sup>Si.

<sup>f</sup> Relative ion intensity ratio normalized for <sup>19</sup>F of positive-ion detection.

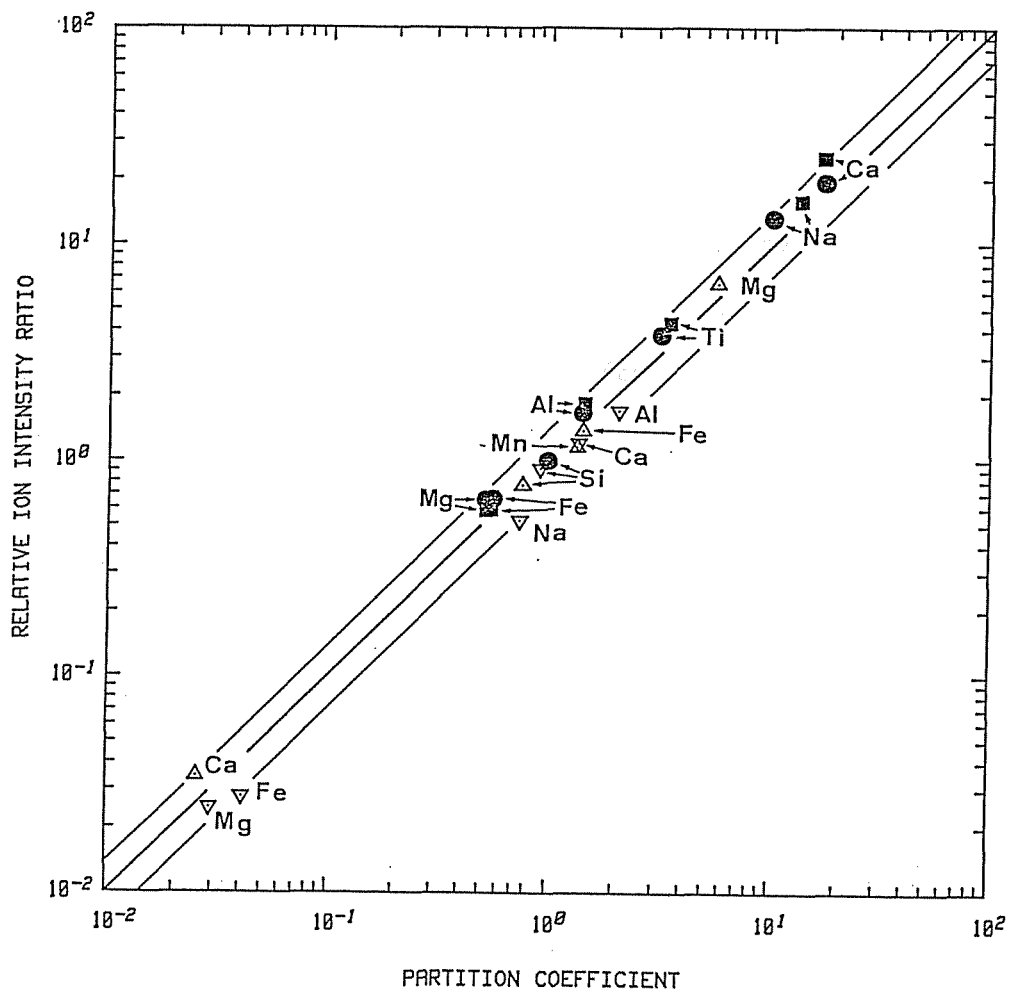


Fig. III-2 The relation between the relative secondary ion intensity and the partition coefficient measured by EPMA.

△: Olivine/groundmass (Yurimoto and Sueno 1984a)

▽: Plagioclase/groundmass (Yurimoto and Sueno 1984a)

●: TKW-03-A (This study)

■: TKW-03-B (This study)



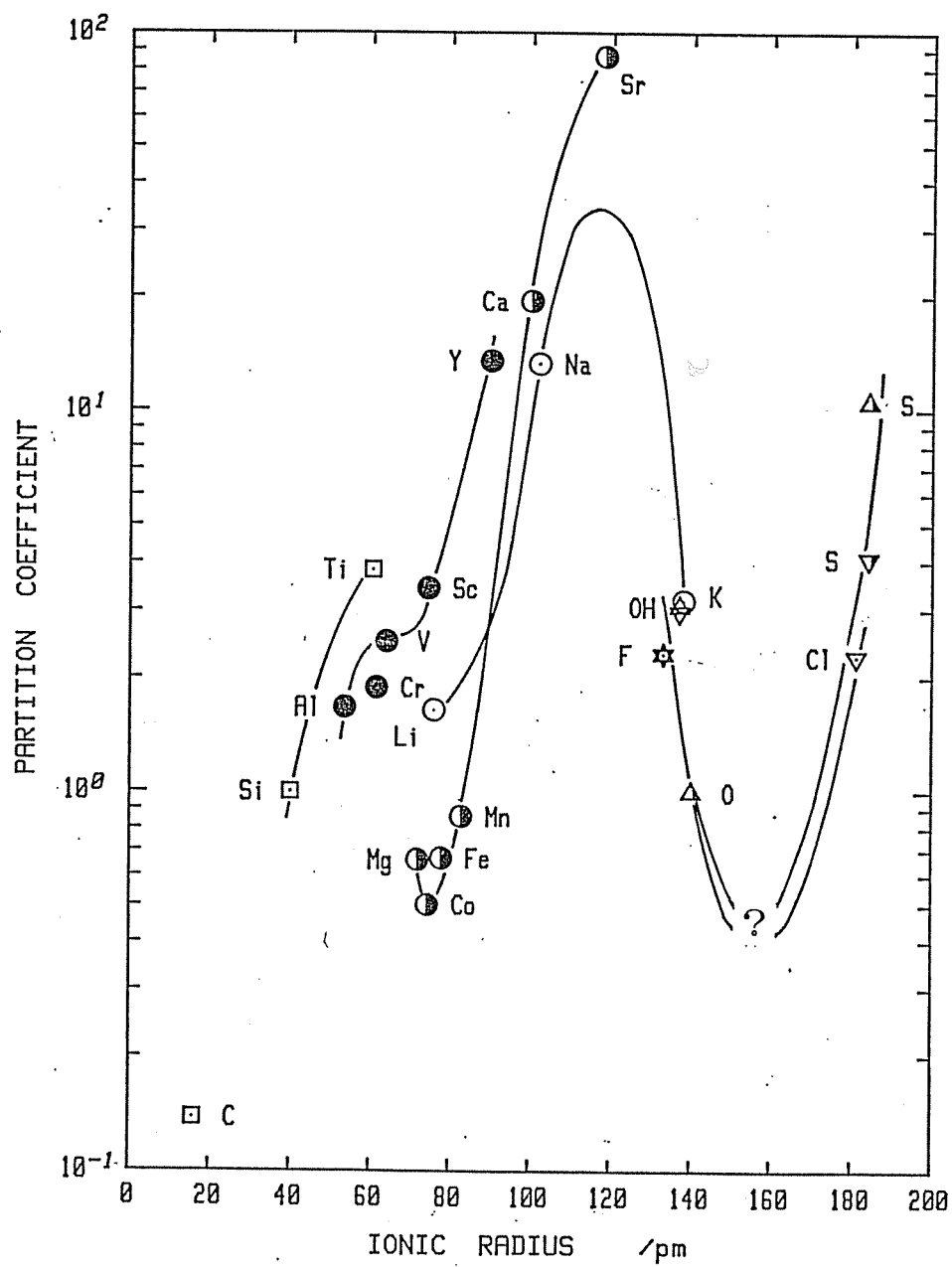


Fig. III-3 Partition coefficient-ionic radius diagram for TKW-03-A.  
 Symbols are the same as in Fig. I-1.

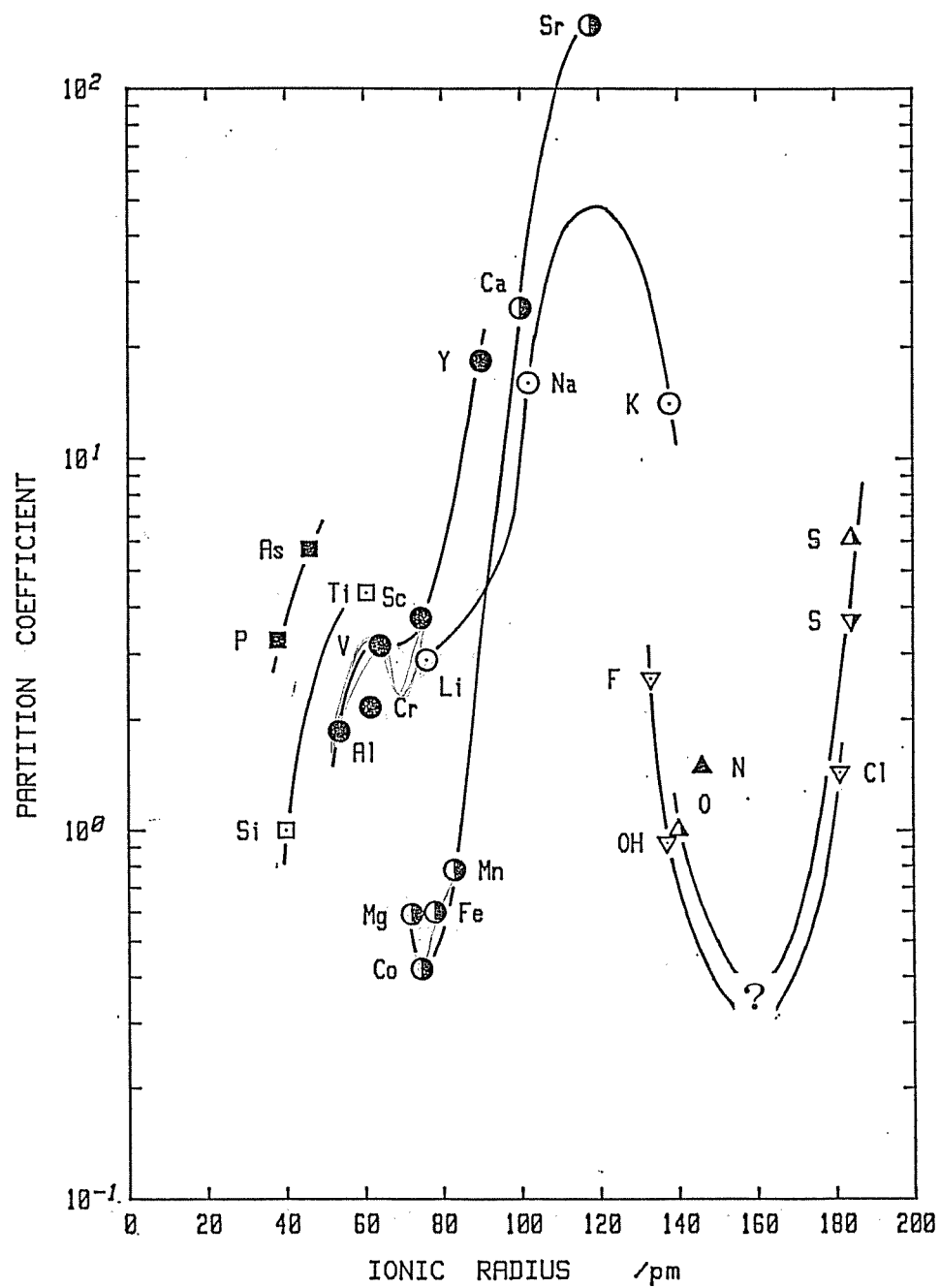


Fig. III-4 Partition coefficient-ionic radius diagram for TKW-03-B.  
 Symbols are the same as in Fig. I-1.

where S and L identify solid and liquid, respectively, k is Boltzman's constant, T and E are the temperature and the internal energy of this system, respectively.  $(\partial E / \partial N_i^S)_P$  is the internal energy change provided by the substitution of an ion of the main component by an ion of a trace component at constant temperature and pressure.

From same assumption and similar procedure given by Nagasawa (1966), we find that the distribution coefficient between A and B phases are given in general as

$$\log K_D^{A/B}(i/j) = - \frac{1}{kT} \left( \frac{\partial E}{\partial N_i^A} \right)_P. \quad (2)$$

In the closed two phase system,

$$N_i^A + N_i^B = \text{constant}. \quad (3)$$

Finally, the distribution coefficient are calculated as

$$\log K_D^{A/B}(i/j) = - \frac{1}{kT} \left\{ \left( \frac{\partial E^A}{\partial N_i^A} \right)_P - \left( \frac{\partial E^B}{\partial N_i^B} \right)_P \right\}. \quad (4)$$

From Eq. 4, one finds that  $K_D^{S/S'}(i/j)$  is controlled by the relative internal energy change provided by the substitution of an ion of the main component by an ion of a trace component between crystal structures of solid S and another solid S' phases. The distribution coefficient  $K_D^{S/L}(i/j)$  can be approximated as a particular example of Eq. 4, i.e., it is only controlled by  $(\partial E^S / \partial N_i^S)_P$ , and,  $(\partial E^L / \partial N_i^L)_P = 0$ , because it appear that the solid/liquid partitioning is under strong control of the crystal structure, and that the peak position on PC-IR diagram is represented the optimum ion size for the crystal (Nagasawa 1966; Onuma

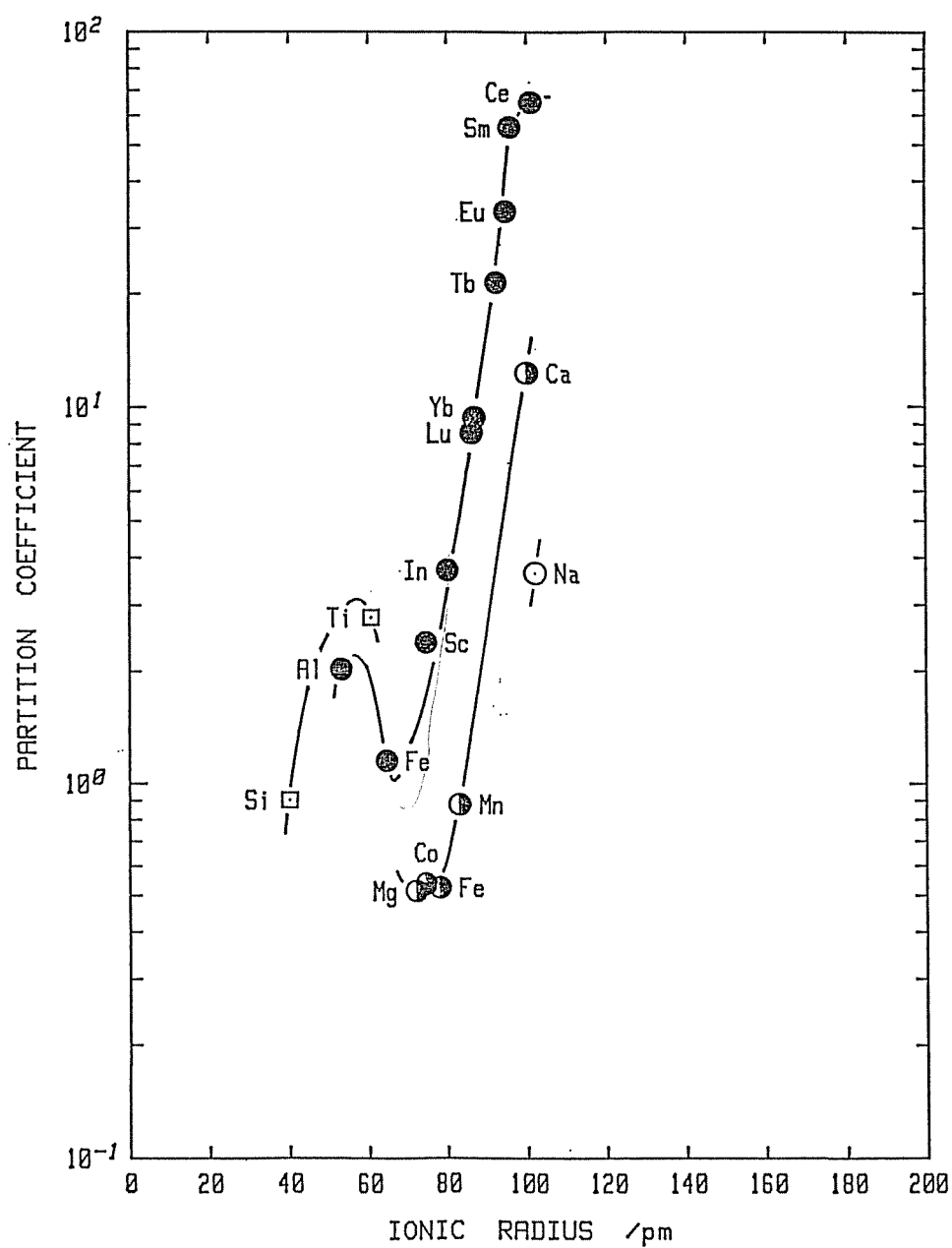


Fig. III-5 Partition coefficient-ionic radius diagram for augite-bronzite phenocrysts (after Matsui et al. 1977). Symbols are the same as in Fig. I-1.

(7) Generally, the partition coefficients between A and B phase may be defined by relative internal energy change provided by the substitution of an ion of the main component (j) by an ion of a trace component (i) between the phases as shown in below:

$$\log K_D^{A/B}(i/j) = - \frac{1}{kT} \left\{ \left( \frac{\partial E^A}{\partial N_i^A} \right)_P - \left( \frac{\partial E^B}{\partial N_i^B} \right)_P \right\}.$$

Arnesen, A. Richard Albert. (1974) The partition coefficients of trace elements between the phases of magmatic rocks.

The partition coefficients of trace elements between the phases of magmatic rocks. Ph.D. thesis, University of Oslo, Norway.

1974, 1975.

Arnesen, R. (1979) The role of trace elements in the differentiation of magmatic rocks.

Arnesen, R. (1979) Trace elements in magmatic rocks. Mineral. Soc. Norway.

1979.

Arnesen, R. (1979) The application of crystal field theory.

Arnesen, R. (1979) Cambridge University Press.

Arnesen, R. (1979) The role of trace elements in the differentiation of magmatic rocks.

Arnesen, R. (1979) The role of trace elements in the differentiation of magmatic rocks.

Arnesen, R. (1979) The role of trace elements in the differentiation of magmatic rocks.

Arnesen, R. (1979) The role of trace elements in the differentiation of magmatic rocks.

Arnesen, R. (1979) The role of trace elements in the differentiation of magmatic rocks.

Arnesen, R. (1979) The role of trace elements in the differentiation of magmatic rocks.

Arnesen, R. (1979) The role of trace elements in the differentiation of magmatic rocks.

Arnesen, R. (1979) The role of trace elements in the differentiation of magmatic rocks.

1979.

Arnesen, R. (1979) The role of trace elements in the differentiation of magmatic rocks.

Arnesen, R. (1979) The role of trace elements in the differentiation of magmatic rocks.

Arnesen, R. (1979) The role of trace elements in the differentiation of magmatic rocks.

- Irving, A. J. (1978) A review of experimental studies of crystal/liquid trace element partitioning. Geochim. Cosmochim. Acta 42, 743-770.
- Jensen, B. B. (1973) Patterns of trace element partitioning. Geochim. Cosmochim. Acta 37, 2227-2242.
- Kobayashi Y, Arai S (1981) Ultramafic nodules in alkali basalt from Taka-shima, Saga prefecture, Japan. Geosci Rept Shizuoka Univ 6:11-24 (in Japanese with English abstract)
- Komatsu, M. (1980) Clinoenstatite in volcanic rocks from the Bonin Islands. Contrib. Mineral. Petrol. 74, 329-338.
- Kuroda, N. and Shiraki, K. (1975) Boninite and related rocks of Chichi-jima, Bonin Islands, Japan. Rept. Fac. Sci. Shizuoka Univ. 10, 145-155.
- Kuroda, N., Shiraki, K. and Urano, H. (1978) Boninite as a possible calc-alkalic primary magma. Bull. Volcanol. 41, 565-575.
- Kuno, H. (1965) Aluminian augite and bronzite in alkali olivine basalt from Taka-shima, North Kyusyu, Japan. In Advancing Frontiers in Geology and Geophysics, Osmania Univ. Press, Hyderad, 205-220.
- Liotard JM, Dupy C (1980) Partage des elements de transition entre clinopyroxene et orthopyroxene-variations avec la nature des roches. Chem Geol 28:307-319
- Matsui Y (1979) An introduction to crystal chemistry of rockforming minerals. In: Matsui Y, Banno S (eds) Geochemistry of rocks and minerals—Material science of the Earth, III, Geoscience 4. Iwanami Shoten, pp 1-62(in Japanese)
- Matsui, Y., Onuma, N., Nagasawa, H., Higuchi, H. and Banno, S. (1977) Crystal structure control in trace element partition between crystal and magma. Bull. Soc. fr. Minéral. Cristallogr. 100, 315-324.

- Morimoto, N. and Gröven, N. (1970) Refinement of the crystal structure of pigeonite. Ame. Mineral. 55, 1195-1209.
- Morimoto, N. and Koto, K. (1969) The crystal structure of orthoenstatite. Zeit. Krist. 129, 65-83.
- Murakami, T., Takeuchi, Y. and Yamanaka, T. (1982) The transition of orthoenstatite to protoenstatite and the structure at 1080°C. Zeit. Krist. 160, 299-312.
- Nagasawa, H. (1966) Trace element partition coefficient in ionic crystals. Science 152, 767-769.
- Nishida, N., Onuma, N. and Ohtsuka, Y. (1979) A classification of several Yamato-74 chondrites. Mem. Natl Inst. Polar Res., Spec. Issue 12, 144-160.
- Ohashi, Y. and Finger, L. W. (1976) The effect of Ca substitution on the structure of clinoenstatite. Carnegie Inst. Wash. Year book 75, 743-748.
- Onuma, N., Higuchi, H., Wakita, H. and Nagasawa, H. (1968) Trace element partition between two pyroxenes and the host lava. Earth Planet. Sci. Lett. 5, 47-51.
- Onuma, N., Ninomiya, S. and Nagasawa, H. (1981) Mineral/groundmass partition coefficients for nepheline, melilite, clinopyroxene and perovskite in melilite-nepheline basalt, Nyiragongo, Zaire. Geochem. J. 15, 221-228.
- Paques-Ledent, M. Th. and Tarte, P. (1974) Vibration studies of olivine-type compounds—II Orthophosphates, -arsenates and -vanadates  $A^I B^{II} X^V O_4$ . Spectrochim. Acta 30A, 673-689.

- Pauling, L. (1929) The principles determining the structures of complex ionic crystals. J. Am. Chem. Soc. 51, 1010-1026.
- Pauling, L. (1960) The Nature of the Chemical Bond, Ithaca, Cornell Univ. Press.
- Philpotts, J. A. (1978) The law of constant rejection. Geochim. Cosmochim. Acta 42, 909-920.
- Ray, G. and Hart, S. R. (1982) Quantitative analysis of silicates by ion microprobe. Int. J. Mass Spec. Ion Phys. 44, 231-255.
- Sasaki, S., Takeuchi, Y., Fujino, K. and Akimoto, S. (1982) Electron-density distributions of three orthopyroxenes,  $\text{Mg}_2\text{Si}_2\text{O}_6$ ,  $\text{Co}_2\text{Si}_2\text{O}_6$ , and  $\text{Fe}_2\text{Si}_2\text{O}_6$
- Sato, H., Aoki, K., Okamoto, K. and Fujita, B. (1978) Petrology and chemistry of basaltic rocks from hole 396b, IPOD/DSDP Leg 46. Initial Rep. Deep Sea Drill. Proj. 46, 115-141.
- Schmitz-Dumont, O., Fendel, H., Hassanein, M. and Weissenfeld, H. (1966) Farbe und konstitution bei anorganischen Feststoffen, 14, Mitt. Die lichtabsorption des zweiwertigen kupfers in oxidischen wirtsgitten. Mh. Chem., 97, 1660-1695.
- Shannon, R. D. (1976) Revised effective ionic radii and systematic studies of interatomic distances in halides and chalcogenides. Acta Cryst. A32, 751-767.
- Shimizu, N., Semet, M. P., and Allègre, C. J. (1978) Geochemical applications of quantitative ion-microprobe analysis. Geochim. Cosmochim. Acta 42, 1321-1334.
- Shimizu, N. and Hart, S. R. (1982) Applications of the ion microprobe to geochemistry and cosmochemistry. Ann. Rev. Earth Planet. Sci. 10, 483-526.



- Shiraki, K., Kuroda, N., Urano, H. and Maruyama, S. (1980)  
 Clinoenstatite in boninites from the Bonin Islands, Japan. Nature,  
 285, 31-32.
- Steele, I. M., Hervig, R. L., Hutcheon, I. D. and Smith, J. V. (1981)  
 Ion microprobe techniques and analyses of olivine and low-Ca  
 pyroxene. Amer. Mineral. 66, 526-546.
- Takeda, H. (1972) Crystallographic studies of coexisting aluminum  
 orthopyroxene and augite of high-pressure origine. J. Geophy. Res.  
 77, 5798-5811.
- Tsang, T., Philpotts, J. A. and Yin, L. (1978) Trace element  
 partitioning between ionic crystal and liquid. J. Phys. Chem.  
Solids 39, 439-442.
- Yamanaka, T. and Takeuchi, Y. (1982) Thermal atomic displacement in the  
 structure of  $MgAl_2O_4$  and silicate spinels. J. Jpn. Assoc. Miner.  
Petrol. Econ. Geol. Spec. Pap. 3, 61-72.
- Yasuda, M., Kitamura, M. and Morimoto, N. (1983) Electron microscopy of  
 clinoenstatite from a boninite and chondrite. Phys. Chem. Minerals,  
 9, 192-196.
- Yurimoto, H., Sueno, S. (1984a) Anion and cation partitioning between  
 olivine, plagioclase phenocrysts and the host magma: A new  
 application of ion microprobe study. Geochem. J. 18, 85-94.
- Yurimoto, H., Sueno, S. (1984b) Mineral/Groundmass partitioning for  
 chrome spinel in boninite. In Benninghoven, A., Okano, J.,  
 Shimizu, R., Werner, H.W. (eds) Secondary ion mass spectrometry  
SIMS IV. Springer-Verlag, Berlin Heidelberg New York Tokyo,  
 pp. 456-459.